

1 **Revisiting the geographical extent of exceptional warmth in the Early Paleogene**
2 **Southern Ocean**

3
4 Frieling, J.^{1§*}, Bohaty, S.M.², Cramwinckel, M.J.¹, Gallagher, S.J.³, Holdgate, G.R.⁴,
5 Reichgelt, T.⁵, Peterse, F.¹, Pross, J.², Sluijs, A.¹, and Bijl, P.K.^{1*}

6
7 ¹ Department of Earth Sciences, Faculty of Geosciences, Utrecht University, Princetonlaan 8a,
8 3584CB, The Netherlands

9 ² Institute of Earth Sciences, Heidelberg University, Im Neuenheimer Feld 234, D-69120 Heidelberg,
10 Germany

11 ³ School of Geography, Earth and Atmospheric Sciences, The University of Melbourne, Melbourne,
12 Australia

13 ⁴ Geotrack International, Brunswick West, Australia

14 ⁵ Department of Geosciences, University of Connecticut, Beach Hall, 354 Mansfield Road, Storrs CT
15 06269, USA

16
17 §Now at: Department of Earth Sciences, University of Oxford, South Parks Road OX1 3AN, UK

18 *Corresponding authors: Joost Frieling (joost.frieling@earth.ox.ac.uk), Peter Bijl (p.k.bijl@uu.nl)
19

20 **Abstract**

21 To assess zonal temperature and biogeographical patterns in the Paleogene of the
22 Southern Ocean, we present new multi-proxy air and sea surface temperature data for
23 the latest Paleocene (~57–56 Ma) and the Paleocene-Eocene Thermal Maximum
24 (PETM; ~56 Ma) from the northern margin of the Australo-Antarctic Gulf (AAG).
25 The various proxies document the well-known late Paleocene gradual warming and,
26 superimposed, two late Paleocene pre-cursor warming events, hundreds of kyrs prior
27 to the PETM. Remarkably, however, air and sea surface temperature reconstructions
28 for the AAG and SW Pacific during the latest Paleocene, PETM and Early Eocene
29 Climatic Optimum (~53–49 Ma) show similar trends and, within proxies, similar
30 absolute temperatures. The record implies that the exceptional warmth previously
31 recorded in the SW Pacific extended westward into the AAG. This contrasts with the
32 modeled circulation and temperature patterns. We suggest that simulations of ocean
33 circulation underestimate heat transport in the SW Pacific due insufficient resolution,
34 not allowing for mesoscale eddy-related heat transport. We argue for a systematic
35 approach to tackle model and proxy biases in marginal marine settings, including
36 assessment of underexplored factors as high-latitude proxy mechanisms to confidently
37 assess temperature in these non-analogue climates.

38

39 **Introduction**

40 Periods of transient warming superimposed on sustained greenhouse climates during
41 the Paleocene and Eocene (early Paleogene; ca. 66–34 Million years ago (Ma)) may
42 be employed as potential analogues for current climate change and potential end-
43 member climate states under unabated carbon emissions (Burke et al., 2018). A
44 negative carbon isotope excursion (CIE), globally recorded in terrestrial and marine
45 sediments, combined with ocean acidification (Zachos et al., 2005; McInerney and
46 Wing, 2011) at the onset of the Paleocene-Eocene Thermal Maximum (PETM; 56
47 Ma) shows the rapid input of thousands of petagrams of ¹³C-depleted C to the
48 exogenic carbon pool (Dickens et al., 1995), providing a geologic analogue to
49 present-day anthropogenic emissions. Several similar, smaller, events appear to have
50 occurred in the late Paleocene and throughout the early Eocene (Cramer et al., 2003;
51 Lauretano et al., 2015; Westerhold et al., 2020) although their climatic expression
52 remains unknown.

53 In recent years, fully coupled climate models have been able to broadly reproduce sea
54 surface and air temperature proxy data for the warmest periods of the Cenozoic
55 (Cramwinckel et al., 2018; Evans et al., 2018; Lunt et al., 2021). Similarly, the
56 models can reproduce the magnitude of extreme transient warming across the PETM
57 (Dunkley Jones et al., 2013; Frieling et al., 2017; Hollis et al., 2019; Zhu et al., 2019;
58 Lunt et al., 2021). This suggests that such models provide accurate reflections of
59 global climate states and meridional gradient changes under high radiative forcing.
60 However, even in simulations where the majority of the reconstructed sea surface
61 temperature (SST) patterns and deep ocean temperatures are consistent with model
62 output throughout the Eocene, absolute temperature reconstructions from several
63 regions, notably the Arctic and the SW Pacific Ocean, and in particular the area
64 around the Tasman Gateway and Zealandia, are still much (>10 °C) warmer than
65 simulations (Frieling et al., 2017; Cramwinckel et al., 2018; Evans et al., 2018; Lunt
66 et al., 2021). In contrast to the reconstructions showing exceptional regional warmth,
67 the Southern Ocean, including the south Pacific Ocean, was likely the dominant locus
68 of cold deep-water formation during much of the Paleogene (Pak and Miller, 1992;
69 Huck et al., 2017), highlighting the importance of resolving the paleoceanography and
70 mechanistic understanding of the enigmatic warmth in and around the SW Pacific
71 (Bijl et al., 2009; Hollis et al., 2009; Douglas et al., 2014).

72 SST estimates from the SW Pacific and the Antarctic margin of the Australo-
73 Antarctic Gulf (AAG) (Figure 1) both consistently exceed 30 °C, and megathermal
74 vegetation elements were established during the PETM and early Eocene climate
75 optimum (EECO; ~53–49 Ma) (Bijl et al., 2009; Sluijs et al., 2011; Carpenter et al.,
76 2012; Pross et al., 2012; Bijl et al., 2013a; Contreras et al., 2013; Contreras et al.,
77 2014; Hollis et al., 2015; Bijl et al., 2021; Huurdeman et al., 2021; Reichgelt et al.,
78 2022). Moreover, dinoflagellate cyst (dinocyst) biogeography suggests surface
79 circulation dominated by low and high latitude-derived current influence in the AAG
80 and SW Pacific (Fig. 1a), respectively (Bijl et al., 2011; Bijl et al., 2013b). These
81 interpretations are broadly supported by modeling efforts (Huber et al., 2004) and
82 such a regional circulation pattern results in consistently higher modeled SST in the
83 northern AAG compared to the southwest (SW) Pacific (e.g. Hollis et al., 2009, Fig.
84 1b). It is noteworthy that although proxy-derived SSTs for the SW Pacific are >10 °C
85 higher than the model-derived SSTs (e.g. Lunt et al., 2021) during the EECO, mean
86 annual air temperature (MAAT) reconstructions can be matched by current models
87 (Lunt et al., 2021; Reichgelt et al., 2022).

88 Regional paleoceanography, especially the gradual opening of the Tasman Gateway
89 (TG), would have affected regional temperature trends through re-routing of warm
90 *versus* cold ocean currents (Cande and Stock, 2004; Bijl et al., 2013a; Sijp et al.,
91 2014; 2016). Recent efforts to constrain the consequence of gradual gateway opening
92 suggest that the regional climatic impact of both the Drake Passage and Tasman
93 Gateway is limited unless both allow relatively deep throughflow simultaneously
94 (Sauermilch et al., 2021), a situation that does not seem to have occurred until *ca.* 26
95 Ma (van de Lagemaat et al., 2021). Therefore, even if a shallow connection existed
96 during the Paleocene and early Eocene (Bijl et al., 2013a), it should have had a
97 negligible impact on paleoceanography and heat transport. On the other hand, in very
98 high resolution model simulations ($<1^\circ$), warm mesoscale eddies reach further south
99 than any current in low-resolution runs, resulting in substantial differences in modeled
100 surface water temperatures in parts of the SW Pacific. Such oceanographic features
101 can presumably reduce the temperature difference between the SW Pacific and the
102 AAG directly surrounding the TG (Nooteboom et al., 2022).

103 Unfortunately, however, no well-dated temperature proxy or biogeographical
104 data from the northern margin of the AAG, presumably the warmest place in this
105 region, are available for some key intervals of the Paleogene; the latest Paleocene (*ca.*
106 57–56 Ma) and the PETM. These periods, along with the EECO, deserve particular
107 attention as they are targeted by community data-model comparison efforts such as
108 DeepMIP (Lunt et al., 2017; 2021 Hollis et al., 2019). However, the absence of data
109 hampers the comparison of temperature on both sides of the Tasman Gateway, the
110 reconstruction of regional oceanography and establishing a regional temperature
111 response pattern. Consequently, in-depth assessment of model performance is limited,
112 which is crucial in light of the apparent proxy-model mismatch.

113 To fill this data gap, we present new multi-proxy SST and MAAT estimates
114 for two expanded late Paleocene-PETM sedimentary archives from the AAG at $\sim 60^\circ\text{S}$
115 paleolatitude (Otway Basin, Victoria, Australia, Fig. 1) (Frieling et al., 2018);
116 Huurdeman et al. 2021). Temperature estimates for the AAG are paired with
117 previously published data from the SW Pacific to assess temperature differences
118 across the Tasman Gateway (Table 1). To reconstruct temperature, we applied novel
119 and established lipid biomarker proxies and palynological tools. We reconstruct
120 MAAT from branched glycerol monoalkyl glycerol tetraethers (brGMGTs) (Baxter et
121 al., 2019; Naafs et al., 2018), the relative abundance of isoprenoid glycerol dialkyl
122 glycerol tetraethers (isoGDGTs) with 5 cyclopentane moieties (GDGT-5) (Naafs et
123 al., 2018), and combine this with new and published nearest living relative (NLR)-
124 based MAAT estimates from pollen and spore assemblages and branched GDGTs
125 (brGDGTs) (Huurdeman et al., 2021). Furthermore, we applied the TEX_{86} to estimate
126 (sub-)surface temperature (Schouten et al., 2002; Kim et al., 2010) and support sea
127 temperature reconstructions by utilizing relative abundances of crenarchaeol-isomer
128 to total crenarchaeol (f(cren ')) (Sinninghe Damsté et al., 2012; O'Brien et al., 2017;
129 Bale et al., 2019). Dinocysts produced by thermophilic dinoflagellates and mangrove
130 palm pollen were used to acquire minimum temperature thresholds.

131

132 **Materials and Methods**

133

134 **Material and Setting**

135 Samples from the Latrobe-1 core ($38^\circ 41' 35''$ S, $143^\circ 09' 00''$ E) and the Point
136 Margaret outcrop (~ 3 km east; $38^\circ 43' 28.8''$ S, $143^\circ 10' 35''$ E) were analyzed. A

137 description of sample collection, lithology and stratigraphy of the section was
138 outlined in Frieling et al., (2018).

139 We focused on the latest Paleocene and PETM (Frieling et al., 2018), and analyzed a
140 total of 114 samples for GDGTs and brGMGTs; 94 for Point Margaret and 20 for the
141 Latrobe-1 core. Detailed dinocyst assemblage data were generated for 90 samples
142 from Point Margaret and 20 samples from the Latrobe-1 core. For the latest Paleocene
143 and PETM, brGDGT-based MAAT estimates were published in Huurdeman et al.,
144 (2021). The analyses performed for Huurdeman et al. (2021) were used for isoGDGTs
145 and brGMGTs here.

146 The sites are represented by shallow-marine deposits, marked by a gradual up-section
147 transition from (pro-)deltaic muddy sandstones to sandy silt and mudstones. The input
148 of terrestrial organic matter, presumably from acidic soils and peats in the hinterland
149 based on the consistent presence of *Sphagnum*-like spores and low brGDGT-based
150 pH, is clearly dominant over marine sources in most section intervals (Frieling et al.,
151 2018; Huurdeman et al., 2021). Sediments were deposited in a subsiding trough
152 system, allowing for rapid and almost continuous sediment accumulation during
153 continental rifting (Sauermilch et al., 2019).

154 The regional oceanography of the SW Pacific in the early Paleogene is thought to be
155 characterized by the Antarctic-derived Tasman Current (TC) in the southernmost
156 sector (Figure 1a, Huber et al., 2004; Bijl et al., 2011; Sauermilch et al., 2019 and
157 references therein). Further north, the influence of the lower-latitude Proto-East
158 Australia Current (PEAC) becomes pronounced. The low latitude Proto-Leeuwin
159 Current (PLC) entered the AAG in the west and extended progressively further east as
160 the AAG widened during the Cenozoic.

161

162 **Palynology**

163 A minimum of 200 and 300 specimens were determined to the species level for
164 dinocysts and terrestrial palynomorphs, respectively, in the palynological materials
165 described by Frieling et al. (2018). Dinocyst taxonomy follows Williams et al., (2017)
166 except for the subfamily Wetzelielloideae, where we follow Bijl et al., (2016). We
167 refer to Huurdeman et al. (2021) for details of the pollen and spore taxonomy. Pollen
168 and spore assemblages of 7 samples from the Latrobe-1 bore and 61 from Point
169 Margaret were used to generate NLR data following methodology as described in
170 (Huurdeman et al., 2021). The occurrence and abundance of temperature-sensitive
171 dinocyst and pollen taxa, including the dinocyst taxa *Apectodinium* spp. (>20 °C) and
172 *Florentinia reichartii* (>25 °C) (Frieling and Sluijs, 2018), as well as the mangrove
173 palm *Nypa* pollen (Reichgelt et al., 2018; Huurdeman et al., 2021) are used as
174 quantitative thresholds to support minimum SST and MAAT constraints, respectively.

175

176 **Organic geochemistry**

177 We quantified isoprenoid and branched GDGT and brGMGT abundances from the
178 ultra high performance liquid chromatography – mass spectrometry (UHPLC-MS)
179 analyses conducted by Huurdeman et al., (2021). For a detailed description of the
180 organic geochemistry methods and brGDGTs, we refer to Huurdeman et al. (2021). In
181 short, a synthetic C₄₆ standard (*m/z* 744) was added to obtain absolute concentrations.
182 A minimum peak area cut-off (3000 units) was applied for individual components,
183 which here typically amounts to absolute concentrations well below 1 ng g⁻¹ dry
184 sediment or ~10 µg g⁻¹ TOC.

185

186 *Mean Annual Air Temperature proxies & brGMGTs*

187 In addition to the MAAT estimates based on brGDGTs and nearest living relative
188 (NLR) from pollen and spore assemblages, which follow the approach described in
189 Huurdeman et al. (2021), we here analyze brGMGT distributions. BrGMGTs are
190 produced by unknown bacteria, and are characterized by an additional covalent C-C
191 bond linking their two alkyl chains (Morii et al., 1998; Schouten et al., 2008). The
192 presence of this bond is thought to improve the stability of the membrane under
193 extreme environmental conditions, such as higher temperature. We identify brGMGT
194 compounds with molecular masses of 1048, 1034 and 1020. In addition to peats
195 (Naafs et al., 2018a) and lake sediments (Baxter et al., 2019), these compounds are
196 also produced and recorded in the marine realm (Liu et al., 2012), particularly in
197 oxygen-minimum zones (Xie et al., 2014). Following the outline in (Sluijs et al.,
198 2020), we use the nomenclature of (Baxter et al., 2019) to identify the compounds
199 utilized by the brGMGTI and HMBT-acyclic (Naafs et al., 2018a). The deep-time
200 application of these indices and the abundance of brGMGTs relative to brGDGTs is
201 explored further here (Fig. 2, Fig. S4-6).

202 We further estimate the abundance of isoprenoid GDGT-5, as a percentage relative to
203 GDGT1-3. The occurrence of GDGT-5 (>1%) is restricted to regions with MAAT of
204 at least 19 °C in present-day acidic peats, a relation that has been applied to Paleogene
205 lignites (Naafs et al., 2018b).

206

207 *Sea surface temperature proxies*

208 Prior to calculating TEX₈₆ values, we test whether isoGDGTs generally align with
209 those observed for the global core-top database of (Kim et al., 2010). Deviation from
210 the core-top data would be indicated by high delta ring index (Δ RI) values (Zhang et
211 al., 2016), implying the standard core top TEX₈₆ calibrations may not yield reliable
212 results. For samples that passed the Δ RI cut-off (<0.3), GDGT-2 over 3 ratios
213 (hereafter [2/3]) are employed to assess whether a substantial fraction of GDGTs were
214 deep-water derived (values above >5, see also Discussion).

215 To gain insight into SST trends from samples with substantial overprints, we employ
216 $f(\text{cren}')$ (Sinninghe Damsté et al., 2012; O'Brien et al., 2017; Bale et al., 2019; Baxter
217 et al., 2021). Crenarchaeol is exclusively produced by Thaumarchaeota (Sinninghe
218 Damsté et al., 2002; De La Torre et al., 2008) and therefore substantially less
219 sensitive to overprints by methanogenic or methanotrophic archaea. In addition,
220 Weijers et al., (2006) already noted that the relative abundance of crenarchaeol in
221 soils is relatively low and decreases with increasing acidity; crenarchaeol rarely
222 exceeds a relative abundance of 10% in acidic soils (pH <6). The same applies to
223 peats and Paleogene lignites, where crenarchaeol rarely exceeds 5% (Naafs et al.,
224 2018; Naafs et al., 2017b). Based on the cyclisation of brGDGTs (quantified in the
225 CBT' index; De Jonge et al., (2014)), we find that soils with low pH (values <5 in
226 Paleocene, ~5.5 during the PETM) dominate the distribution at our site (Huurdeman
227 et al., 2021). Collectively, despite high BIT, the brGDGTs appear predominantly
228 derived from acidic soils and peats which makes it likely that the majority of
229 crenarchaeol in our samples is derived from marine Thaumarchaeota and not soils
230 (Fig. S8). We therefore propose that $f(\text{cren}')$ may provide supporting information on
231 relative SST changes in setting with very high terrestrial GDGT input (Frieling et al.,
232 2018; Huurdeman et al., 2021) based on the link between temperature and $f(\text{cren}')$ in
233 cultures as well as the modern core-top calibration dataset (Schouten et al., 2002; Kim
234 et al., 2010; Tierney and Tingley, 2015; Bale et al., 2019). In the core-top data, SST
235 explains a substantial part of the variability in $f(\text{cren}')$ (linear $R^2 = 0.6$) in waters with
236 an SST above 10 °C, although this is slightly less than the traditional TEX₈₆ (linear R^2

237 = 0.75) in the same dataset (Schouten et al., 2002; Tierney and Tingley, 2015)(Fig.
238 S1). The basis of temperature dependency of $f(\text{cren}')$ may be the result of membrane
239 adaptation within Thaumarcheota populations, as the stereoisomer results in slightly
240 different membrane packing (Schouten et al., 2013; Sinninghe Damsté et al., 2018;
241 Bale et al., 2019). In the natural environment, the temperature dependency may also
242 originate from shifts in the Thaumarcheotal populations as has been observed in
243 lacustrine records (Baxter et al., 2021). In the latter case, the positive temperature
244 correlation may come from more dominant (sub-)surface dwelling Thaumarchaeota
245 group I.1b (proportionally high cren') relative to group I.1a (proportionally low cren'),
246 for example due to changing oxygenation, stratification or nutrient distribution within
247 the water column (Baxter et al., 2021). However, strains of Thaumarchaeota group
248 I.1b have so far not been detected in the marine environment. Regardless of the exact
249 mechanism, at nearby ODP Site 1172 (Sluijs et al., 2011; Bijl et al., 2021), virtually
250 all variation in TEX_{86} is captured ($R^2 = 0.98$; Fig. S3) by $f(\text{cren}'$) across the PETM.
251 Together with the correlation to TEX_{86} and SST in the modern core-top dataset, this
252 gives confidence that we can here use $f(\text{cren}'$) to trace SST trends, albeit without
253 coupling this to absolute SST values.

254

255 **Data compilation for the Southern Ocean**

256 We focus on late Paleocene, PETM and EECO marine and terrestrial temperature
257 proxy records for the Southern Ocean, ranging from New Zealand in the southwest
258 Pacific Ocean in the east, towards the AAG in the west, between paleolatitudes of 50°
259 S and 65° S (Seton et al., 2012; Müller et al., 2019) (Fig. 1, Table 1). Both
260 quantitative (GDGT-based proxies, foraminiferal Mg/Ca, NLR-based estimates) and
261 semi-quantitative / qualitative (temperature-indicative dinocyst and mangrove palm
262 pollen) temperature information is incorporated. Absolute temperatures are compared
263 within proxies, within the selected time slices. Time-slices “latest Paleocene” (57–56
264 Ma) and “PETM” (~55.9 Ma) were identified based on carbon-isotope data ($\delta^{13}\text{C}$) if
265 available (i.e., for ODP Site 1172 and DSDP Site 277) and/or on pollen-based
266 biostratigraphy. We here use records from the upper *Lygistepollenites balmei* zone
267 and the *Spinizonocolpites prominatus* subzone to represent the latest Paleocene and
268 PETM, respectively. Consequently, the included Paleocene data have an maximum
269 age of ~57 Ma (Frieling et al., 2018), in compliance with previous compilations and
270 DeepMIP (Dunkley Jones et al., 2013; Frieling et al., 2017; Hollis et al., 2019). Only
271 data comprising the ‘body’, the stable period of anomalously low $\delta^{13}\text{C}$ within the
272 PETM CIE were used, in order to focus on the period of sustained peak warmth.
273 Consequently, the rapid onset and more gradual recovery of the CIE, i.e., with $\delta^{13}\text{C}$
274 values, and potentially temperature, intermediate between background and peak
275 PETM values, were not included. A broad interval covering the EECO, ca. 53–49 Ma,
276 as defined by (Westerhold et al., 2018) previously identified by bio-, magneto- and
277 isotope stratigraphy is used for the EECO data compilation (Hollis et al., 2019). As it
278 is often challenging to assign absolute ages for terrestrial deposits, we also include
279 localities that were determined to be “Ypresian” and “Early Eocene” in age (Hollis et
280 al., 2019).

281

282 **Results**

283

284 *Mean annual air temperature estimates for the northern Australo-Antarctic Gulf*

285

286 *BrGDGTs*

287 Distributions of brGDGTs in sediments from Point Margaret are generally
288 indistinguishable from those in modern soils and peats, with negligible riverine or
289 marine sedimentary contributions throughout the entire succession (Huurdean et al.
290 2021 and supplement thereof). We here extended the brGDGT-based MAAT
291 estimates for the entire late Paleocene part of the Point Margaret section (Fig. 2).
292 There is a long-term warming trend (~ 4 °C) from ~ 18 °C to 22 °C from the top of the
293 section to the onset of the PETM warming around 50.8m. We find two minor pre-
294 cursor warming events around ~ 33 m and 46 m, also supported by other proxies
295 (NLR, $f(\text{cren}')$, dinocysts), superimposed on the long-term trend. Potentially similar
296 fluctuations further down section (e.g. ~ 27 m, Fig. S9) in brGDGT-based MAAT
297 cannot be confirmed as warming events as these fluctuations are not mimicked by
298 similar signals in other proxies.

299
300

Isoprenoid GDGT-5

301 In the Point Margaret sediments we find abundant GDGT-5. The occurrence and
302 abundance of this compound in our shallow marine setting is likely explained by
303 substantial input of peat-derived material, consistent with the presence of *Sphagnum*
304 spores (Huurdean et al. 2021). Although there is substantial scatter and a few ($n =$
305 13) samples without GDGT-5 throughout the section, GDGT-5 is mostly present ($n =$
306 81) and comprises up to $\sim 10\%$ of the isoGDGT assemblage (GDGTs 1-3), close to the
307 maximum percentage observed for modern tropical peats (Fig. 2, Fig. S9). In the
308 upper part of the section, %GDGT-5 reaches a maximum of 3% on a relatively stable
309 latest Paleocene (43-50m height) average $\sim 1.5\%$. In this interval, %GDGT-5 appears
310 to broadly follow brGDGT-derived temperatures.

311 However, as GDGT-1 to 3, used to calculate %GDGT-5, are also derived from marine
312 Thaumarcheota and possibly other non-terrestrial sources (Fig. S4, S8), the calculated
313 %GDGT-5 for all our samples must be regarded as a minimum estimate of the
314 original source. Considering the calculated terrestrial fraction of GDGT-1 to 3 is ~ 30 -
315 50% (Supp. Data) in some late Paleocene intervals, the relative abundance of GDGT-
316 5 in the source material could well have been similar to, or higher than some modern
317 tropical peats (Naafs et al., 2018). A single-point within the body of the CIE reaches
318 $\sim 6\%$ GDGT-5 (Fig. 2E). However, it is difficult to gauge the value of this
319 observation: starting from the onset of the CIE, %GDGT-5 and *Sphagnum* spores are
320 no longer consistently present, implying that most of the source material is lost, or at
321 least does not always reach the site.

322
323

BrGMGTs

324 The Point Margaret section yields a suite of brGMGTs that have recently been
325 documented in peats (Naafs et al., 2018a), Paleogene lignites (Naafs et al., 2018a),
326 and African lakes (Baxter et al., 2019) and both modern marine surface (Liu et al.,
327 2012) and Paleogene marine sediments (Sluijs et al., 2020; Bijl et al., 2021). Naafs et
328 al. (2018a) show that the relative abundance of brGMGTs over regular brGDGTs is
329 positively correlated with MAAT in peats. In the Point Margaret section, the amount
330 of brGMGTs relative to brGDGTs is positively correlated to MBT'_{5Mc}-based MAAT,
331 but is marked by higher values ($>10\%$ of total brGDGTs) than all modern peat
332 samples at the same MAAT (Fig. S5). This may signal that we significantly
333 underestimate absolute temperatures or that additional sources, for example marine
334 (sedimentary) organisms, add brGMGTs in our setting (Baxter et al., 2021; Kirkels et
335 al., 2022). Baxter et al. (2019) calibrated the brGMGT distributions, formulated as the
336 brGMGT-index (brGMGTI), in tropical lake sediments to temperature. Although the

337 application of the brGMGTI proxy outside tropical lakes is unvalidated, we note that
338 the brGMGT-derived MAAT response at our site is somewhat greater than that based
339 on regular brGDGTs (Fig. 2D). We also find high scatter in this proxy in some
340 intervals (particularly around the onset of the PETM CIE, 49-51m), which may
341 suggest the mixing of different brGMGT sources, likely peat and *in situ* marine.
342 Despite the relatively limited range of temperature covered in our data, the HMBT-
343 acyclic (Naafs et al., 2018a) shows a strong correlation with e.g. MBT'_{5Me} and f(cren')
344 (Fig. S7, Supp. Text). However, accurately assigning variability to either air or sea
345 surface temperature, or another, indirect control is difficult without proper source
346 identification (Kirkels et al., 2022). Collectively, it is noteworthy that both HMBT-
347 acyclic and brGMGTI follow MBT'_{5Me} MAAT trends and that brGMGTI produces
348 similar MAAT despite the lack of an environment-specific calibration.
349

350 *Terrestrial palynomorphs and NLRs*

351 The expanded late Paleocene record (0–47m) yields relatively high MAAT (~18 °C)
352 considering its paleolatitude between 55 and 65° S. These late Paleocene NLRs of the
353 pollen and spore taxa align well with estimates from the upper part of the Point
354 Margaret section (Hurdeman et al. 2021) and Latrobe-1 (this study). NLR-based
355 MAATs are 17–19.8 °C (median: 18.1 °C) for the late Paleocene. MAAT estimates
356 from the lower part of the section (2–30m) yield values around 17°C, and slightly
357 higher (~18°C) in the upper part of the succession (30–48m), with subtle increases
358 signaling pre-cursor warming events (~33m and ~46m) also observed in brGDGT-
359 based MAAT estimates. A ~3–4 °C rise in MAAT was previously calculated for the
360 PETM (Hurdeman et al. 2021).

361 Aside from the nearest living relative approach to estimate MAAT, we use the well-
362 known climatic envelopes of fossil pollen taxa such as *Spinizonocolpites prominatus*
363 (*Nypa*), a mangrove palm that only occurs in regions with MAAT >22 °C at present
364 (Reichgelt et al., 2018). This species has a first consistent appearance at 50.57 m at
365 Point Margaret (Fig. 2F), 23 cm below the CIE onset (Hurdeman et al., 2021), and
366 occurs within the PETM CIE body (299.67 m below surface) and the EECO in the
367 Latrobe-1 core (Frieling et al., 2018). The presence of *Nypa* implies that coastal
368 MAAT was at least 22 °C in the northern AAG just prior to and during the PETM and
369 during the EECO.

370

371 *Sea surface temperature estimates for the northern Australo-Antarctic Gulf*

372 *TEX₈₆*

373 We generated new isoGDGT data for the Point Margaret outcrop and Latrobe-1
374 borehole. The isoGDGT distributions in most samples from the Point Margaret
375 section and the Latrobe-1 bore have ΔRI values >0.3 signaling non-pelagic
376 contributions to the isoGDGT pool (Zhang et al., 2016). In most samples, soil-derived
377 isoGDGT input, as indicated by the branched and isoprenoid tetraether (BIT) index
378 and contributions from methanogenic and methanotrophic isoGDGT producers, as
379 derived from the Methane Index (MI) exceeded generally proposed cut-offs (0.3–0.4
380 for BIT (Hopmans et al., 2004; Weijers et al., 2007) and 0.3 for MI (Zhang et al.,
381 2011)). Concentrations in the Latrobe-1 samples are <1 ng g⁻¹ sediment or <10 mg g⁻¹
382 total organic carbon (TOC) for most compounds, generally sufficient to identify, but
383 not properly quantify, isoGDGTs, and insufficient to identify penta- and
384 hexamethylated brGDGTs and brGMGTs. This implies that brGDGT distributions
385 could not be used to estimate mean annual air temperature for these samples. We also
386 note that the recorded concentrations are remarkably low compared to the sediments

387 from the nearby (~3 km) Point Margaret, which may be the result of oxidation during
388 long-term (40–50 year) dry storage. A similar effect was noted for dinocysts (Frieling
389 et al., 2018).

390

391 Excluding samples with high ΔRI , only 5 samples at Point Margaret were identified
392 as suitable to calculate TEX_{86} -derived SST, of which 4 are from the PETM CIE. A
393 single late Paleocene data point with $\Delta RI < 0.3$ yielded a TEX_{86} value of 0.66, and
394 although this sample does pass the ΔRI cut-off, it is marked by a very high BIT index
395 value (0.76). Similarly, two late Paleocene high-BIT index samples from the Latrobe-
396 1 core with low GDGT-3 abundances (< 3000 peak area, typically $< 0.5 \text{ ng g}^{-1}$
397 sediment for GDGT-3), had otherwise normal isoGDGT-distributions based on ΔRI
398 values (< 0.3) and yielded TEX_{86} values of 0.67. However, as the concentrations of
399 most isoGDGTs and brGDGTs approach the analytical limits and potentially have
400 high terrestrial isoGDGT contributions, the resulting TEX_{86} values must be viewed
401 with caution as the analytical error is larger than for other samples and indices.
402 Absolute SST estimates based on TEX_{86}^H (Kim et al., 2010) are $\sim 27 \text{ }^\circ\text{C}$ for the late
403 Paleocene and $\sim 32 \text{ }^\circ\text{C}$ during the PETM, implying a 5–6 $^\circ\text{C}$ warming during the
404 PETM.

405

406 $f(\text{cren}')$

407 In the Point Margaret section, we further constrain the temperature trends in the
408 marine realm using the fractional abundance of the crenarchaeol stereoisomer relative
409 to total crenarchaeol ($f(\text{cren}')$) (Fig. 2B). Similar to the data from ODP 1172, in Point
410 Margaret, $f(\text{cren}')$ shows a strong linear relation with the scarce TEX_{86} data ($R^2 =$
411 0.96 , $p = 0.002$, $n = 5$) and broadly reproduces the long-term rise in brGDGT- and
412 NLR-derived temperatures in the late Paleocene (0–50 m), as well as the two late
413 Paleocene transient precursor warming episodes (~ 33 and 46m) (Fig. 2B, 2F). The
414 precursor warming events are pronounced in $f(\text{cren}')$, whereas the response in
415 brGDGTs and NLR appears more subdued.

416 Moreover, $f(\text{cren}')$ rises just before (50.57 m) the onset of the CIE (50.8 m), whereas
417 the rise in MBT'_{5Me} slightly lags the CIE (~ 51 m). SST rise directly prior to the CIE,
418 as recorded here in $f(\text{cren}')$, has also been recognized elsewhere (Thomas et al., 2002;
419 Sluijs et al., 2007; Secord et al., 2010; Frieling et al., 2019). The presumed
420 temperature signal obtained from $f(\text{cren}')$ is supported by the coeval appearance of
421 mangrove palm pollen (Hurdeman et al., 2021, Fig. 2F). The delayed response (up to
422 a few kyr) in brGDGT-based MAAT compared to vegetation-derived MAAT was
423 attributed by Hurdeman et al. (2021) to 1) differences in transport time and/or 2)
424 reworking of Paleocene or even older soil materials (John et al., 2012) and clay-bound
425 organics (Schneider-Mor and Bowen, 2013), including brGDGTs. This may result in
426 an apparent delay in warming in peat and soil-derived components (brGDGTs, and
427 (peat-derived) brGMGTs) while warming based on above ground vegetation
428 (palynomorphs), especially coastal elements (mangrove palms) and marine
429 compounds ($f(\text{cren}')$, dinocysts), would be more synchronous with the warming. It
430 might be these processes also played a role in suppressing the temperature change
431 inferred from brGDGTs relative to other proxies during the precursor warming
432 events.

433

434 *Dinocysts*

435 Late Paleocene and PETM SST trends as reconstructed through $f(\text{cren}')$ are supported
436 by progressively higher percentages of thermophilic dinocysts towards the top of the

437 Paleocene section (Fig. 2C), even though these taxa are outnumbered by low-salinity
438 tolerant taxa during pre-CIE warming and onset of the PETM CIE (ca. 50–50.9 m,
439 Fig. S9). In addition to rough trends, the appearance and relative abundance of
440 selected extinct thermophilic dinocysts, notably *Apectodinium* spp. and *Florentinia*
441 *reichartii* provide constraints on minimum SST. The first abundance events of
442 *Apectodinium* (>10%) are found during the precursor warming events in the latest
443 Paleocene (at ~33 m and ~46 m, Fig. 2C) at Point Margaret. These events are not
444 registered in the Latrobe-1 core, which may be due to low sampling resolution and/or
445 poor recovery in the respective core intervals. A third abundance increase is recorded
446 at Point Margaret during the CIE, which is mirrored by a similar event in the Latrobe-
447 1 core (SI; Fig. S10). *F. reichartii* is never abundant (maximum: 5% at Point
448 Margaret), and occurs consistently only during peak CIE. A single late Early Eocene
449 (EECO) abundance event of *Apectodinium* is found in the Latrobe-1 core (pers. obs. J.
450 Frieling). Following observations of Frieling and Sluijs, (2018) we arrive at most
451 likely minimum SST estimates ~20–25 °C for the latest Paleocene (based on
452 occasional *Apectodinium* abundance; Latrobe-1 core and Point Margaret), 25–30 °C
453 for the PETM (based on *F. reichartii*) for the Point Margaret section and 20–25 °C for
454 the EECO in the Latrobe-1 core. The relative abundance of these thermophilic taxa
455 follows the long-term late Paleocene SST rise, as well as short-term variations (Fig. 2)
456 observed in other temperature proxies (f(cren'), MBT'_{5Me}, brGMGTI) in detail except
457 for a short interval around the CIE onset at Point Margaret.

458

459 **Integrated regional SST for the AAG and SW Pacific (Table 1)**

460 The early Paleogene climate of the SW Pacific has been intensely studied with a
461 range of proxies (Hollis et al., 2019). The majority of SST data is based on TEX₈₆,
462 and secondly planktonic foraminiferal Mg/Ca ratios. Briefly, the SW Pacific TEX₈₆^H
463 and Mg/Ca records show SSTs of ~26–30 °C in the late Paleocene (Table 1), rising to
464 31–33 °C during the PETM. For the EECO, results are somewhat more variable and
465 carbonate-based proxies show somewhat lower temperatures on average (~26 °C)
466 compared to TEX₈₆^H (31–32 °C) (Hollis et al., 2019).

467 Fewer data were available for the AAG and prior to this study, none for the late
468 Paleocene and PETM. Although some caution is warranted due to high BIT in our
469 samples, the new data suggest that TEX₈₆-based SSTs in the late Paleocene (27 °C),
470 PETM (~32 °C) and the published data from Site U1356A (32 °C) were
471 indistinguishable from those in the SW Pacific in the same intervals.

472 This is supported by semi-quantitative lines of evidence, particularly the occurrence
473 and abundance of thermophilic dinocysts; the abundance of *Apectodinium* and
474 occurrence of *F. reichartii* during the PETM are mirrored east and west of the
475 Tasman Gateway (Figure 3, 4). Similarly, high SSTs during the EECO of U1356 are
476 accompanied by high relative abundances of *Apectodinium*.

477

478 **Integrated regional mean air temperatures for the AAG and SW Pacific (Table 1)**

480 For the SW Pacific, MAATs have been reconstructed for several localities, but, due to
481 the nature of the proxies, a relatively small number of samples per location compared
482 to SSTs. Available Late Paleocene MAAT reconstructions for the SW Pacific region
483 are mostly vegetation-based (e.g. NLR, leaf margin analyses) approaches. This
484 includes localities Konkon-1 and Poonboon-1 in the Bass Basin (e.g. Contreras et al.,
485 2014), and Cambalong Creek, on the southeast Australian coast (Greenwood et al.,
486 2003) (Fig. 1), ODP Site 1172 and Mid-Waipara, New Zealand, which together arrive

487 at an average of ~16 °C, with MAAT rising to ~20 °C during the PETM. The EECO
488 MAAT estimates are based on brGDGT-based proxy applications from ODP Site
489 1172 (Bijl et al., 2013a; Bijl et al., 2021) and Mid-Waipara (Pancost et al., 2013), and
490 yield MAAT of ~21–22 °C.

491 Within the AAG realm, late Paleocene MAAT reconstructions are now available for
492 the Point Margaret outcrop (Huurdeeman et al., 2021; this study) and Latrobe-1 (this
493 study). The abundance of GDGT-5 in the latest Paleocene of the Point Margaret
494 outcrop indicates MAAT >19 °C, the NLR-based estimates (Latrobe-1 & Point
495 Margaret) arrive at 16–19 °C and the Point Margaret brGDGT-based estimates are 21–
496 22 °C. Both NLR and MBT'_{5Me} indicate a MAAT rise during the PETM, to 20–22°C
497 and 23°C, respectively. BrGMGTI derived MAAT estimates suggests slightly higher
498 temperatures during the PETM (~24 °C) and a temperature increase comparable to
499 NLR-based estimate (~4 °C), although these results should be treated with some
500 caution, as brGMGTI estimates were only calculated for Point Margaret and this
501 novel proxy remains largely untested. MAAT estimates for the EECO are derived
502 from only few localities (Table 1). This includes Lowana Road, also known as
503 Regatta Point, in the Sorrell Basin, western Tasmania, IODP Site U1356A on the
504 Antarctic Margin and two recent ensemble (NLR and leaf-morphology) estimates
505 from Dinmore and Deans Marsh, Australia (Reichgelt et al., 2022). The localities
506 show somewhat divergent plant-based MAAT estimates; NLR shows MAAT ~18 °C
507 at U1356A, while a higher MAAT is reconstructed for Lowana Road (~24°C). The
508 ensemble MAAT estimates from Dinmore and Deans Marsh fall between these
509 estimates. BrGDGT-based estimates from U1356A align with the average of all
510 vegetation-based estimates (~20–21 °C). Similar to the SST estimates, MAAT
511 estimates from the SW Pacific and AAG within the same proxy are indistinguishable
512 for the same intervals.

513 Terrestrial micro- and macrofossil evidence paint a very similar picture: mangrove
514 palm pollen (*Nypa*) are found throughout the entire studied area during the PETM
515 (Fig. 4) and also appear during the EECO (e.g. Latrobe-1 core (J. Frieling pers. obs.)
516 and Lowana Road (Carpenter et al., 2012)).

517

518 **Discussion**

519 *Late Paleocene warming events*

520 Multiple temperature proxies reflect two late Paleocene transient warming events
521 superimposed on subtle long-term warming (Fig. 2). These events do not seem to be
522 local. The second pre-cursor warming (PW-2) at ~46m in the Point Margaret section
523 has an equivalent at ODP Site 1172 (Fig. 3). This may also hold true for the event at
524 ~33m, although at ODP Site 1172 only very subtle increases in *Apectodinium*
525 abundance (~613.2 and ~615.5 m below sea floor) are found (Bijl et al., 2021). Based
526 on average late Paleocene accumulation rates at ODP Site 1172 (0.6 cm kyr⁻¹; Sluijs
527 et al., 2011) and Point Margaret (average ~7 cm kyr⁻¹; Frieling et al., 2018), PW-2
528 may precede the PETM by some 100 kyr, and by extrapolation, this would imply PW-
529 1 at 33m is perhaps another ~200 kyr older but we note that in marginal settings
530 sedimentation rates can strongly vary on short time-scales. Although their exact
531 timing remains unclear, this is an interval in which only minor deep ocean carbon
532 isotope fluctuations occur (Cramer et al., 2003; Westerhold et al., 2018; Westerhold et
533 al., 2020). Given current constraints on their age, PW-1 and 2 appear to precede
534 previously recognized precursor carbon isotope events that occur much closer to the
535 PETM CIE (e.g. Bowen et al., 2015; Babila et al., 2022). Although it may be argued a

536 subtle decrease in $\delta^{13}\text{C}_{\text{org}}$ co-occurs with the precursor warmings, this could also
537 result from coeval small changes in organic matter sourcing. We hence find no solid
538 evidence for any CIE occurring at the same level as either of the transient precursor
539 warming events.

540 However, even if the relation of these subtle transient warming events to the
541 variability recorded in the deep ocean is difficult to constrain, these events are
542 noteworthy as they exceed the (regional) variability observed in most of the
543 Paleocene (Fig. 2). Although these events can only be revealed in high-resolution data
544 generated for background climates, such data is currently scarce. Yet, resolving such
545 signals from background noise, could prove essential to understand (Paleogene)
546 climate and carbon cycle behavior (Sluijs et al., 2007; Bowen et al., 2015; Armstrong
547 McKay and Lenton, 2018).

548

549 *Potential for brGMGT proxies*

550 Collectively, we find that the strong correlations with other reconstructed
551 environmental parameters including MAAT and SST support a temperature-related
552 response in brGMGTs. However, their common presence in lakes, peats and marine
553 sediments implies that it is challenging to accurately assign observed variability to
554 either air or sea surface temperature, or other parameters indirectly related to
555 temperature (Kirkels et al., 2022). Despite this, we note that both HMBT and
556 brGMGTI follow MBT'_{5Me}-based MAAT trends and brGMGTI produces similar
557 absolute MAAT estimates despite the lack of an environment-specific calibration.

558 Intriguingly, the HMBT not only corresponds in trend with MBT'_{5Me}-MAAT, but the
559 ratios between the compounds (brGMGTs 1020 / 1020 + 1034 + 1048) are also
560 virtually identical with the traditional MBT(acyclic; defined as brGDGT-Ia /
561 brGDGT-Ia + IIa + IIIa including their 6-methyl counterparts (Weijers et al., 2007)),
562 supporting the notion that these compounds have a shared origin and/or mechanistic
563 purpose in microbial membranes. In addition, the increase in brGMGT abundance
564 relative to that of regular brGDGTs (%brGMGT) across the onset of the CIE may
565 imply that the formation of H-shaped compounds represents an additional temperature
566 adaptation (Morii et al., 1998; Naafs et al., 2018a) and/or that production of
567 brGMGTs increased relative to that of brGDGTs in specific (i.e. marine) source areas
568 (Kirkels et al., 2022). Despite these unknowns, the clear correlation to reconstructed
569 environmental parameters and the ubiquitous presence of brGMGTs in these
570 (shallow) marine settings such as sampled at Point Margaret highlight the potential
571 for new paleoenvironment proxies based on brGMGTs once their origin and function
572 are better resolved.

573

574 *No temperature differences between the Australo-Antarctic Gulf and the Southwest 575 Pacific?*

576 We find identical absolute temperatures, both marine and terrestrial, within proxies
577 and temperature trends in the AAG and the SW Pacific for all analyzed intervals (i.e.,
578 late Paleocene, PETM and EECO; Fig. 4). This could be assumed consistent with the
579 similar paleolatitudes of the investigated sites (60–65°S). However, it is difficult to
580 reconcile with the proposed large-scale ocean circulation patterns, i.e., the warm low-
581 latitude PLC in the AAG and cooler higher-latitude TC in the SW Pacific, across the
582 analyzed interval (Fig. 1). It also contrasts with modeled differences in SST and
583 MAAT between the areas east and west of the Tasman Gateway.

584 It is remarkable that not only the trends (Fig. 3), but also the reconstructed
585 absolute TEX₈₆-based temperatures are similar across analyzed sections in the marine

586 realm (Fig. 4). While a seasonality bias in SST proxies could affect latitudinal
587 gradients through dominance of warm-season productivity at higher latitudes (e.g.
588 Antoine et al., 1996), it is unlikely that such effects would eliminate zonal differences
589 (Fig. 4). Modern examples, such as the SST difference between the eastern and
590 western North Atlantic that can exceed 5° C (e.g. Gouretski and Koltermann, 2004),
591 support the notion that substantial zonal differences, such as those expected across the
592 Tasman Gateway, should be detectable in proxy data.

593 One aspect that warrants exploration is the contribution of deep-water derived
594 isoGDGTs and their potential impact on TEX₈₆-derived temperature reconstructions.
595 While isoGDGT-producing Thaumarcheota occur through the entire water column,
596 their highest concentrations are generally found near the lower part of the mixed
597 layer, in the nitrite maximum, around 50–150m depth (e.g. Pitcher et al., 2011; Hurley
598 et al., 2016; Hurley et al., 2018). The contribution of deep-water derived isoGDGTs
599 can be assessed using [2/3] (e.g. Taylor et al., 2013; Kim et al., 2015; Hurley et al.,
600 2018), which is based on the observation that [2/3] in suspended particulate matter
601 (SPM) increases rapidly below 150-200m depth ([2/3] of ~3 up to ~200m depth, ~25
602 at >200m depth) (e.g. Hernández-Sánchez et al., 2014; Hurley et al., 2018). Low [2/3]
603 are observed for the TEX₈₆ datasets used here: Point Margaret (average 2), ODP1172
604 (2.5–3.5 for Paleocene-Eocene, 2.6 for EECO), Mid-Waipara (2.5), Hampden Beach
605 (1.6) and U1356A (1.6), which, at face value, suggests contribution of deep-water
606 derived isoGDGTs were minor. We therefore find [2/3] differences between the
607 localities used here do not reveal any obvious differences in isoGDGT production
608 depths.

609 The reconstructed temperatures and trends for the AAG relative to those in the
610 SW Pacific increase the geographical extent of the discrepancy between modeled and
611 proxy-derived temperatures in the high southern latitudes (Hollis et al., 2012; Lunt et
612 al., 2021). At the same time, the findings for the AAG imply that the model-data
613 discrepancy is not limited to the SW Pacific, but extends into the AAG (Lunt et al.,
614 2021). Moreover, this zonal pattern did not notably change during intervals of both
615 transient (PETM) and multi-million-year global warming (Late Paleocene-EECO).
616 The temperature patterns exist within the marine and terrestrial realms and are evident
617 in fundamentally different proxies for both realms. This seems to reinforce the
618 existence of anomalously high SSTs in the AAG and particular the SW Pacific and it
619 appears unlikely that the discrepancy can be resolved by an improved mechanistic
620 understanding of a single SST proxy. While the MAAT for both regions, as for SST
621 proxies, is indistinguishable, the absolute reconstructed MAATs are often *ca.* 10 °C
622 below SST (see also e.g. Bijl et al., 2021) and in relatively close agreement with
623 modeled MAAT at high *p*CO₂ (e.g. Lunt et al., 2021; Reichgelt et al., 2022).

624 It remains uncertain how accurate the reconstructed absolute mean annual
625 temperatures from the individual proxies are. For example, culture experiments
626 emulating the non-analogue high-latitude conditions, such as the seasonal contrasts in
627 light conditions in combination with high-temperature, are yet lacking. Constraining
628 proxy behavior under climate conditions such as those that prevailed in the high
629 southern latitudes during the early Paleogene might prove crucial to assess the value
630 of currently available and forthcoming data. In the following section, we explore and
631 revisit new and previously proposed options that may merit further attention in order
632 to improve our understanding of deep-time high-latitude climate.

633
634

Spatial biases in the proxy and modeled temperature signals

635 In general, the inherent heterogeneity of hinterlands and, by extension, sourcing and
636 transport of terrestrial components, particularly pollen and spores, gives rise to several
637 challenges and may complicate a robust comparison between localities (e.g. Inglis et
638 al., 2019). Challenges include changes in the catchment area, including vegetation
639 source, river flow path, coastal proximity, altitude, and spatial integration. While this
640 may affect some interpretations that rely on whole assemblages or presence/absence
641 data (NLR), we suggest that this is likely a relatively minor issue for lowland or
642 coastal taxa and indeed much of the study area. We find this assumption is warranted
643 by the apparently synchronous appearance of *Nypa* across the TG, the relatively short
644 time span of the studied time interval, and the fact that all records come from passive
645 margins, implying that major tectonic changes in the catchment area are unlikely.
646 However, comparing to localities further offshore or regions with strong (paleo)relief
647 will invariably include some of these factors.

648 As the above factors mostly affect terrestrial proxy data, it is unlikely that
649 invoking one single effect (e.g., seasonal biases, sourcing) resolves much of the
650 model-data discrepancy. However, until recently, one effect on marine temperature
651 proxies may have been largely overlooked. There is a dominance of records from
652 near-shore, shallow and coastal environments in the compilation, an inherent
653 (preservation) bias of many deep-time temperature reconstructions. Modern marginal
654 marine settings generally experience greater influence of nearby landmasses and,
655 partly as a consequence, more pronounced seasonal SST variations (~10 °C)
656 compared to open marine or oceanic (typically <5 °C) (Hirahara et al., 2014; Judd et
657 al., 2020), and it is reasonable to assume this was similar in the Paleogene. A greater
658 mean annual temperature range potentially exacerbates any seasonal bias that may
659 exist in proxy data for example by further amplifying warm-season dominated proxy
660 signals.

661 Lastly, the low-resolution (1° and greater) models the (paleo)climate modeling
662 community relies on tend to strongly over- or underestimate temperature in specific
663 regions due to lack of fine-scale oceanographic features such as meso-scale eddies.
664 The effects of this are most pronounced in regions associated with eastern and
665 western boundary currents (Judd et al., 2020). Comparing the, mostly near-shore,
666 paleoclimate reconstructions to low horizontal resolution model simulations may be
667 complicated by such effects (Judd et al., 2020; Nooteboom et al., 2021), especially for
668 regions with complex (paleo)geography. As these factors are challenging to constrain,
669 and impact is likely to be site-specific it is difficult to gauge whether and how this
670 may influence our ability to constrain and compare regional temperature patterns.

671 *Influence of paleogeography*

672 On a global scale and over latitudinally averaged zones, climate models can now
673 reproduce proxy data (Cramwinckel et al., 2018; Evans et al., 2018), but an accurate
674 representation of the global, local and regional paleogeography becomes important for
675 finer scale model-data comparisons (Lunt et al., 2016; Frieling et al., 2017;
676 Nooteboom et al., 2020; Nooteboom et al., 2021). The paleogeography of the region
677 around the Tasman Gateway includes many continental blocks of uncertain
678 paleobathymetry (Williams et al., 2019), which means that even if fully coupled
679 simulations were to be run in higher spatial resolution, uncertainty in
680 paleobathymetry/paleogeography may still impact temperature distribution. However,
681 extreme end-member early Paleogene (prior to *ca.* 50 Ma) TG geographies with either
682 deep throughflow or high topography have predictable climatic and oceanographic
683 consequences (Bijl et al., 2011; Sijp et al., 2011; Sijp et al., 2016; Sauermilch et al.,
684

685 2021) that remain unsupported by the combination of tectonic, biogeographic and
686 temperature proxy data (Baatsen et al., 2018). This implies that such drastic changes
687 in paleogeographic boundary conditions are not primary candidates to resolve the
688 regional discrepancy between data and models.

689 Although the paleobathymetry of the SW Pacific itself has received less
690 attention than Southern Ocean gateways (Lagabrielle et al., 2009; Bijl et al., 2013a;
691 van de Lagemaat et al., 2021), recent work has suggested that sectors of the now
692 submerged continental plates of Zealandia may have been shallow or even emerged
693 above sea level during the Paleogene (Sutherland et al., 2019). The exact influence of
694 bathymetric features on the surface and deep ocean flow and heat distribution in this
695 region is yet unknown, but likely important for the exact configuration and shape of
696 the South Pacific polar gyre and thereby the direction of the proto-East-Australian
697 Current, as has been argued for other regions of deep-water formation (Coxall et al.,
698 2018; Vahlenkamp et al., 2018).

699 Apart from regional or local details in paleogeography, the use of either a
700 hotspot or paleo-magnetic reference frame for absolute paleolatitude reconstructions
701 may have a large impact on modeled oceanography at the sites used in this study. The
702 type of framework does not notably affect the positions of the sites relative to each
703 other, but the paleomagnetic framework shifts localities around the TG ca. 5 (± 5)°
704 latitude north (Seton et al., 2012; van Hinsbergen et al., 2015; Müller et al., 2019), so
705 relative to the spin axis of the Earth. While this may seem trivial, much of the region
706 is within a latitudinal band that is highly sensitive to such changes (Baatsen et al.,
707 2020). Specifically, placing the same regional geography at lower latitudes implies
708 that there is a higher probability of wind-driven surface currents entering the
709 Australo-Antarctic Gulf and the SW Pacific through the Proto-Leeuwin current (PLC)
710 and Proto East-Australia current (PEAC), respectively, an effect that is independent of
711 model resolution (Baatsen et al., 2018; Nooteboom et al., 2021). Ultimately, the
712 minor shifts in paleolatitude may therefore have major impact on the origin and
713 temperature of water masses bathing sites east of the TG.

714

715 *Low-latitude current invasion into the SW Pacific and Australo-Antarctic Gulf*

716 Intriguingly, recent high-resolution (0.1°) ocean model simulations show an invasive
717 PEAC in the middle Eocene, penetrating as far south as ~55° S (Nooteboom et al.,
718 2021), bringing it within reach of some SW Pacific sites (e.g. DSDP 277, New
719 Zealand) unlike previous simulations (e.g., Huber et al., 2004; Hollis et al., 2012). A
720 shallow connection between the AAG and the SW Pacific may have existed in the
721 early Paleogene and would be in line with a superficial similarity of the dinocyst
722 assemblages from ODP Site 1172 and Point Margaret and Latrobe-1. However,
723 dinocyst bioprovinces are generally not well-defined in the Paleocene and earliest
724 Eocene, with the majority of taxa likely having a cosmopolitan distribution (e.g.
725 Frieling and Sluijs, 2018), implying similarity on either side did not necessitate an
726 open Tasman Gateway and associated warm or cold through flow.

727 While the observed biogeographic separation in the Middle and Late Eocene
728 (Huber et al., 2004; Bijl et al., 2011; Cramwinckel et al., 2020) may be interpreted as
729 the expression of a temperature or oceanographic difference, most modern and extinct
730 dinocysts, including thermophilic taxa such as *Apectodinium* have a wide temperature
731 tolerance (Prebble et al., 2013; Zonneveld et al., 2013; Frieling and Sluijs, 2018).
732 Therefore, it is much more likely that a combination of local environmental
733 parameters, including, for example, nutrient availability, coastal proximity and
734 salinity (Bijl et al., 2021), ultimately determined the assemblage characteristics and

735 therefore regional biogeography (Bijl et al., 2011; Zonneveld et al., 2013). In this
736 sense, previous interpretations of corresponding modeled high or low SST and
737 biogeography may have overstated the influence of SST on dinocyst biogeography.

738 With the currently available evidence from emergent high-resolution (0.1°)
739 ocean model runs we consider “warm”-current invasion into the SW Pacific and AAG
740 as the leading mechanism for forcing similar temperatures east and west of the
741 Tasman Gateway. This however does not yet explain the extremely high temperatures
742 in the high-latitude AAG or SW Pacific. Particularly temperatures from SST proxies
743 remain difficult to obtain from models that for other regions and MAAT proxies
744 produce similar results.

745

746 **Conclusions**

747 The southwest Pacific Ocean (~50–60°S paleolatitude) was anomalously warm
748 through much of the early Paleogene, and proxy SSTs exceed modeled SST by ~10
749 °C. Our data extend the area with extremely high proxy temperatures westward into
750 the AAG, with broad implications for reconstruction of meridional temperature
751 gradients and polar amplification that would be based on zonally averaged
752 temperature or temperature patterns and general ocean circulation.

753 The new multi-proxy temperature records from the AAG reveal a long-term
754 Late Paleocene warming on land and in the ocean, and, superimposed, two Late
755 Paleocene transient ‘precursor’ warming events, some ~300–400 and ~100 kyr prior
756 to the PETM. The origin, geographical extent and magnitude of these transient events
757 remain uncertain, but the existence of such relatively pronounced (regional)
758 variability is remarkable.

759 The new data also emphasizes the persistence of high, but similar absolute
760 temperatures and temperature evolution on both sides of a likely closed Tasman
761 Gateway through the warmest periods of the Paleogene (late Paleocene, PETM and
762 EECO). A strong influence of low-latitude ocean currents on both sides of the
763 Tasman Gateway is not expected based on marine microfossil distributions or low-
764 resolution models, yet should not be discarded as a mechanism that contributed to
765 excessive regional warmth and particularly similar temperatures east and west of the
766 TG.

767 A scenario with (seasonal) low-latitude influences on both sides of the Tasman
768 Gateway may become a preferred scenario when high-resolution (eddy-resolving)
769 modeling can be shown to accurately represent surface water conditions in the
770 Paleocene-Eocene Southern Ocean. Moreover, the difference between low and high-
771 resolution climate model runs may shed some light on SST over- or underestimates
772 east and west of the Tasman Gateway. In addition, a more accurate representation of
773 seasonality in the coastal-marginal marine settings may aid in resolving the influence
774 of proxy biases.

775 However, even if part of the model-data discrepancy can be resolved by higher-
776 resolution climate modeling, including an accurate representation of paleogeography,
777 it is likely other challenges, such as the offset between SST and MAAT estimates,
778 still limit our understanding of these distinctly non-analogue climates as they
779 prevailed in the southern mid to high-latitudes. Some of these directly complicate
780 comparison of proxy data to climate models, such as the influence of paleogeographic
781 and paleobathymetric boundary conditions; factors that are both difficult to
782 reconstruct and to accurately represent in models.

783

784 **Acknowledgments**

785 We thank G. Dammers, E.P. Hurdeman, K. Nierop, C. Rem and A. van Leeuwen for
786 assistance in palynological processing and organic geochemical analyses. E. Hopmans
787 is thanked for assistance and discussions on UHPLC-MS data. E.P. Hurdeman is
788 acknowledged for work on the Latrobe-1 core as part of a Master's thesis. SJG was
789 supported by the Australian IODP office. JP acknowledges support by the German
790 Research Foundation (DFG; grant PR 651/24-1). AS thanks the European Research
791 Council for consolidator grant #771497. PKB acknowledges support from NWO
792 Vernieuwingsimpuls Veni grant no 863.13.002.

793

794 **Data availability**

795 All newly generated data has been submitted and will be available via the Pangaea
796 database upon publication (DOI to be added).

797

798
799
800
801
802
803
804
805
806
807
808
809
810
811
812
813
814
815
816
817
818
819
820
821
822
823
824
825
826
827
828
829
830
831
832
833
834
835
836
837
838
839
840
841
842
843
844
845
846
847
848
849
850
851
852
853
854
855
856
857

References

- Antoine, D., Andrt, J.M., and Morel, A., 1996, Oceanic primary production: 2. Estimation at global scale from satellite (Coastal Zone Color Scanner) chlorophyll: *Global Biogeochemical Cycles*, v. 10, no. 1, p. 57–69, doi: 10.1029/95GB02832.
- Armstrong McKay, D.I., and Lenton, T.M., 2018, Reduced carbon cycle resilience across the Palaeocene–Eocene Thermal Maximum: *Climate of the Past*, v. 14, no. 10, p. 1515–1527, doi: 10.5194/cp-14-1515-2018.
- Baatsen, M., von der Heydt, A.S., Huber, M., Kliphuis, M.A., Bijl, P.K., Sluijs, A., and Dijkstra, H.A., 2018, Equilibrium state and sensitivity of the simulated middle-to-late Eocene climate: *Climate of the Past Discussions*, , no. April, p. 1–49, doi: 10.5194/cp-2018-43.
- Baatsen, M., Von Der Heydt, A.S., Huber, M., Kliphuis, M.A., Bijl, P.K., Sluijs, A., and Dijkstra, H.A., 2020, The middle to late Eocene greenhouse climate modelled using the CESM 1.0.5: *Climate of the Past*, v. 16, no. 6, p. 2573–2597, doi: 10.5194/cp-16-2573-2020.
- Babila, T.L., Penman, D.E., Standish, C.D., Doubrava, M., Bralower, T.J., Robinson, M.M., Self-trail, J.M., Speijer, R.P., Stassen, P., Foster, G.L., and Zachos, J.C., 2022, Surface ocean warming and acidification driven by rapid carbon release precedes Paleocene-Eocene Thermal Maximum: v. 1025, no. March, p. 1–14.
- Bale, N.J., Palatinszky, M., Rijpstra, W.I.C., Herbold, C.W., Wagner, M., and Damsté, J.S.S., 2019, Membrane lipid composition of the moderately thermophilic ammonia-oxidizing archaeon “*Candidatus Nitrosotenuis uzonensis*” at different growth temperatures: *Applied and Environmental Microbiology*, v. 85, no. 20, doi: 10.1128/AEM.01332-19.
- Baxter, A.J., van Bree, L.G.J., Peterse, F., Hopmans, E.C., Villanueva, L., Verschuren, D., and Sinninghe Damsté, J.S., 2021, Seasonal and multi-annual variation in the abundance of isoprenoid GDGT membrane lipids and their producers in the water column of a meromictic equatorial crater lake (Lake Chala, East Africa): *Quaternary Science Reviews*, v. 273, doi: 10.1016/j.quascirev.2021.107263.
- Baxter, A.J., Hopmans, E.C., Russell, J.M., Sinninghe, J.S., Sinninghe Damsté, J.S., and Sinninghe, J.S., 2019, Bacterial GMGTs in East African lake sediments: Their potential as palaeotemperature indicators: *Geochimica et Cosmochimica Acta*, doi: 10.1016/j.gca.2019.05.039.
- Bijl, P.K., Bendle, J.A.P., Bohaty, S.M., Pross, J., Schouten, S., Tauxe, L., Stickley, C.E., McKay, R.M., Rohl, U., Olney, M., Sluijs, A., Escutia, C., Brinkhuis, H., Klaus, A., et al., 2013a, Eocene cooling linked to early flow across the Tasmanian Gateway: *Proceedings of the National Academy of Sciences*, v. 110, no. 24, p. 9645–9650, doi: 10.1073/pnas.1220872110.
- Bijl, P.K., Brinkhuis, H., Egger, L.M., Eldrett, J.S., Frieling, J., Grothe, A., Houben, A.J.P., Pross, J., Śliwińska, K.K., and Sluijs, A., 2016, Comment on ‘Wetzeliella and its allies – the “hole” story: a taxonomic revision of the Paleogene dinoflagellate subfamily Wetzelielloideae’ by Williams et al. (2015): *Palynology*, v. 6122, no. January 2017, p. 1–7, doi: 10.1080/01916122.2016.1235056.
- Bijl, P.K., Frieling, J., Cramwinckel, M.J., Boschman, C., Sluijs, A., and Peterse, F., 2021, Maastrichtian-Rupelian paleoclimates in the southwest Pacific – a critical evaluation of biomarker paleothermometry and dinoflagellate cyst paleoecology at Ocean Drilling Program Site 1172: *Climate of the Past*, , no. March, p. 6, doi: 10.5194/cp-2021-18.
- Bijl, P.K., Pross, J., Warnaar, J., Stickley, C.E., Huber, M., Guerin, R., Houben, A.J.P., Sluijs, A., Visscher, H., and Brinkhuis, H., 2011, Environmental forcings of Paleogene Southern Ocean dinoflagellate biogeography: *Paleoceanography*, v. 26, no. 1, p. 1–12, doi: 10.1029/2009PA001905.
- Bijl, P.K., Schouten, S., Sluijs, A., Reichert, G.-J., Zachos, J.C., and Brinkhuis, H., 2009, Early Palaeogene temperature evolution of the southwest Pacific Ocean: *Nature*, v. 461, no. 7265, p. 776–779, doi: 10.1038/nature08399.
- Bijl, P.K., Sluijs, A., and Brinkhuis, H., 2013b, A magneto- and chemostratigraphically calibrated dinoflagellate cyst zonation of the early Palaeogene South Pacific Ocean: *Earth-Science Reviews*, v. 124, no. 0, p. 1–31, doi: http://dx.doi.org/10.1016/j.earscirev.2013.04.010.
- Bowen, G.J., Maibauer, B.J., Kraus, M.J., Röhl, U., Westerhold, T., Steimke, A., Gingerich, P.D., Wing, S.L., and Clyde, W.C., 2015, Two massive, rapid releases of carbon during the onset of the Palaeocene-Eocene thermal maximum: *Nature Geoscience*, v. 8, no. 1, p. 44–47.
- Burke, K.D., Williams, J.W., Chandler, M.A., Haywood, A.M., Lunt, D.J., and Otto-Bliesner, B.L., 2018, Pliocene and Eocene provide best analogs for near-future climates: *Proceedings of the National Academy of Sciences*, p. 201809600, doi: 10.1073/pnas.1809600115.
- Cande, S.C., and Stock, J.M., 2004, Cenozoic reconstructions of the Australia-New Zealand-South Pacific sector of Antarctica, *in* *Geophysical monograph series*, p. 5–17.

858 Carpenter, R.J., Jordan, G.J., Macphail, M.K., and Hill, R.S., 2012, Near-tropical early eocene
859 terrestrial temperatures at the Australo-Antarctic margin, western Tasmania: *Geology*, v. 40, no.
860 3, p. 267–270, doi: 10.1130/G32584.1.

861 Contreras, L., Pross, J., Bijl, P.K., Koutsodendris, A., Raine, J.I., van de Schootbrugge, B., and
862 Brinkhuis, H., 2013, Early to Middle Eocene vegetation dynamics at the Wilkes Land Margin
863 (Antarctica): *Review of Palaeobotany and Palynology*, v. 197, p. 119–142, doi:
864 10.1016/j.revpalbo.2013.05.009.

865 Contreras, L., Pross, J., Bijl, P.K., O’Hara, R.B., Raine, J.I., Sluijs, A., and Brinkhuis, H., 2014,
866 Southern high-latitude terrestrial climate change during the Palaeocene–Eocene derived from a
867 marine pollen record (ODP Site 1172, East Tasman Plateau): *Climate of the Past*, v. 10, no. 4, p.
868 1401–1420.

869 Coxall, H.K., Huck, C.E., Huber, M., Lear, C.H., Legarda-Lisarri, A., O’Regan, M., Sliwiska, K.K.,
870 Van De Fliedrt, T., De Boer, A.M., Zachos, J.C., and Backman, J., 2018, Export of nutrient rich
871 Northern Component Water preceded early Oligocene glaciation /704/106/413
872 /704/829 /704/106/2738 article: *Nature Geoscience*, v. 11, no. 3, p. 190–196, doi:
873 10.1038/s41561-018-0069-9.

874 Cramer, B.S., Wright, J.D., Kent, D. V., and Aubry, M.-P., 2003, Orbital climate forcing of d13C
875 excursions in the late Paleocene-early Eocene (chrons C24n-C25n): *Paleoceanography*, v. 18, no.
876 4, p. 21.

877 Cramwinckel, M.J., Huber, M., Kocken, I.J., Agnini, C., Bijl, P.K., Bohaty, S.M., Frieling, J., Goldner,
878 A., Hilgen, F.J., Kip, E.L., Peterse, F., van der Ploeg, R., Röhl, U., Schouten, S., et al., 2018,
879 Synchronous tropical and polar temperature evolution in the Eocene: *Nature*, v. 559, no. 7714, p.
880 382–386, doi: 10.1038/s41586-018-0272-2.

881 Cramwinckel, M.J., Woelders, L., Hurdeman, E.P., Peterse, F., Gallagher, S.J., Pross, J., Burgess,
882 C.E., Reichart, G.J., Sluijs, A., and Bijl, P.K., 2020, Surface-circulation change in the southwest
883 Pacific Ocean across the Middle Eocene Climatic Optimum: Inferences from dinoflagellate cysts
884 and biomarker paleothermometry: *Climate of the Past*, v. 16, no. 5, p. 1667–1689, doi:
885 10.5194/cp-16-1667-2020.

886 Crouch, E.M., Willumsen, P.S., Kulhanek, D.K., and Gibbs, S.J., 2014, A revised Paleocene (Teurian)
887 dinoflagellate cyst zonation from eastern New Zealand: *Review of Palaeobotany and Palynology*,
888 v. 202, p. 47–79, doi: 10.1016/j.revpalbo.2013.12.004.

889 Dickens, G.R., O’Neil, J.R., Rea, D.K., and Owen, R.M., 1995, Dissociation of oceanic methane
890 hydrate as a cause of the carbon isotope excursion at the end of the Paleocene:
891 *Paleoceanography*, v. 10, no. 6, p. 965–971, doi: 10.1029/95PA02087.

892 Douglas, P.M.J., Affek, H.P., Ivany, L.C., Houben, A.J.P., Sijp, W.P., Sluijs, A., Schouten, S., and
893 Pagani, M., 2014, Pronounced zonal heterogeneity in Eocene southern high-latitude sea surface
894 temperatures.: *Proceedings of the National Academy of Sciences of the United States of*
895 *America*, v. 111, no. 18, p. 1–6, doi: 10.1073/pnas.1321441111.

896 Dunkley Jones, T., Lunt, D.J., Schmidt, D.N., Ridgwell, A.J., Sluijs, A., Valdes, P.J., and Maslin,
897 M.A., 2013, Climate model and proxy data constraints on ocean warming across the Paleocene–
898 Eocene Thermal Maximum: *Earth-Science Reviews*, v. 125, no. 0, p. 123–145, doi:
899 <http://dx.doi.org/10.1016/j.earscirev.2013.07.004>.

900 Evans, D., Sagoo, N., Renema, W., Cotton, L.J., Müller, W., Todd, J.A., Saraswati, P.K., Stassen, P.,
901 Ziegler, M., Pearson, P.N., Valdes, P.J., and Affek, H.P., 2018, Eocene greenhouse climate
902 revealed by coupled clumped isotope-Mg/Ca thermometry: *Proceedings of the National*
903 *Academy of Sciences*, v. 115, no. 6, p. 1174–1179, doi: 10.1073/pnas.1714744115.

904 Frieling, J., Gebhardt, H., Huber, M., Adekeye, O.A., Akande, S.O., Reichart, G.-J., Middelburg, J.J.,
905 Schouten, S., and Sluijs, A., 2017, Extreme warmth and heat-stressed plankton in the tropics
906 during the Paleocene-Eocene Thermal Maximum: *Science Advances*, v. 3, no. 3, p. e1600891,
907 doi: 10.1126/sciadv.1600891.

908 Frieling, J., Hurdeman, E.P., Rem, C.C.M., Donders, T.H., Pross, J., Bohaty, S.M., Holdgate, G.R.,
909 Gallagher, S.J., McGowran, B., and Bijl, P.K., 2018, Identification of the Paleocene–Eocene
910 boundary in coastal strata in the Otway Basin, Victoria, Australia: *Journal of*
911 *Micropalaeontology*, v. 37, no. 1, p. 317–339, doi: 10.5194/jm-37-317-2018.

912 Frieling, J., Peterse, F., Lunt, D.J.J., Bohaty, S.M.M., Damsté, J.S.S., Reichart, G. -J. -J., Sluijs, A.,
913 Sinninghe Damsté, J.S., Reichart, G. -J. -J., and Sluijs, A., 2019, Widespread Warming Before
914 and Elevated Barium Burial During the Paleocene-Eocene Thermal Maximum: Evidence for
915 Methane Hydrate Release? *Paleoceanography and Paleoclimatology*, p. 2018PA003425, doi:
916 10.1029/2018PA003425.

917 Frieling, J., and Sluijs, A., 2018, Towards quantitative environmental reconstructions from ancient

918 non-analogue microfossil assemblages: Ecological preferences of Paleocene – Eocene
919 dinoflagellates: *Earth-Science Reviews*, v. 185, no. August, p. 956–973, doi:
920 10.1016/j.earscirev.2018.08.014.

921 Gouretski, V.V., and Koltermann, K.P., 2004, WOCE Global Hydrographic Climatology: Berichte des
922 Bundesamtes für Seeschifffahrt und Hydrographie, doi: 10.5065/GS51-V170.

923 Greenwood, D.R., Moss, P.T., Rowett, A.I., Vadala, A.J., and Keefe, R.L., 2003, Plant communities
924 and climate change in southeastern Australia during the early Paleogene, *in* Special Paper 369:
925 Causes and consequences of globally warm climates in the early Paleogene, Geological Society
926 of America, p. 365–380.

927 Hernández-Sánchez, M.T., Woodward, E.M.S., Taylor, K.W.R., Henderson, G.M., and Pancost, R.D.,
928 2014, Variations in GDGT distributions through the water column in the South East Atlantic
929 Ocean: *Geochimica et Cosmochimica Acta*, v. 132, p. 337–348, doi: 10.1016/j.gca.2014.02.009.

930 Hines, B.R., Hollis, C.J., Atkins, C.B., Baker, J.A., Morgans, H.E.G., and Strong, P.C., 2017,
931 Reduction of oceanic temperature gradients in the early Eocene Southwest Pacific Ocean:
932 Palaeogeography, Palaeoclimatology, Palaeoecology, v. 475, p. 41–54, doi:
933 10.1016/j.palaeo.2017.02.037.

934 van Hinsbergen, D.J.J., de Groot, L. V., van Schaik, S.J., Spakman, W., Bijl, P.K., Sluijs, A., Langereis,
935 C.G., and Brinkhuis, H., 2015, A Paleolatitude Calculator for Paleoclimate Studies: *PloS one*, v.
936 10, no. 6, p. e0126946, doi: 10.1371/journal.pone.0126946.

937 Hirahara, S., Ishii, M., and Fukuda, Y., 2014, Centennial-scale sea surface temperature analysis and its
938 uncertainty: *Journal of Climate*, v. 27, no. 1, p. 57–75, doi: 10.1175/JCLI-D-12-00837.1.

939 Hollis, C.J., Dunkley Jones, T., Anagnostou, E., Bijl, P.K., Cramwinckel, M.J., Cui, Y., Dickens, G.R.,
940 Edgar, K.M., Eley, Y., Evans, D., Foster, G.L., Frieling, J., Inglis, G.N., Kennedy, E.M., et al.,
941 2019, The DeepMIP contribution to PMIP4: methodologies for selection, compilation and
942 analysis of latest Paleocene and early Eocene climate proxy data, incorporating version 0.1 of the
943 DeepMIP database: *Geoscientific Model Development*, v. 12, no. 7, p. 3149–3206, doi:
944 10.5194/gmd-12-3149-2019.

945 Hollis, C.J., Handley, L., Crouch, E.M., Morgans, H.E.G., Baker, J.A., Creech, J., Collins, K.S., Gibbs,
946 S.J., Huber, M., Schouten, S., Zachos, J.C., and Pancost, R.D., 2009, Tropical sea temperatures
947 in the high-latitude South Pacific during the Eocene: *Geology*, v. 37, no. 2, p. 99–102, doi:
948 10.1130/G25200A.1.

949 Hollis, C.J., Hines, B.R., Littler, K., Villasante-Marcos, V., Kulhanek, D.K., Strong, C.P., Zachos, J.C.,
950 Eggins, S.M., Northcote, L., and Phillips, A., 2015, The Paleocene–Eocene Thermal Maximum
951 at DSDP Site 277, Campbell Plateau, southern Pacific Ocean: *Climate of the Past*, v. 11, no. 7, p.
952 1009–1025, doi: 10.5194/cp-11-1009-2015.

953 Hollis, C.J., Taylor, K.W.R., Handley, L., Pancost, R.D., Huber, M., Creech, J.B., Hines, B.R., Crouch,
954 E.M., Morgans, H.E.G., Crampton, J.S., Gibbs, S., Pearson, P.N., and Zachos, J.C., 2012, Early
955 Paleogene temperature history of the Southwest Pacific Ocean: Reconciling proxies and models:
956 *Earth and Planetary Science Letters*, v. 349–350, p. 53–66, doi: 10.1016/j.epsl.2012.06.024.

957 Hopmans, E.C., Weijers, J.W.H., Schefuß, E., Herfort, L., Sinninghe Damsté, J.S., and Schouten, S.,
958 2004, A novel proxy for terrestrial organic matter in sediments based on branched and isoprenoid
959 tetraether lipids: *Earth and Planetary Science Letters*, v. 224, no. 1–2, p. 107–116, doi:
960 10.1016/j.epsl.2004.05.012.

961 Huber, M., Brinkhuis, H., Stickley, C.E., Döös, K., Sluijs, A., Warnaar, J., Schellenberg, S.A., and
962 Williams, G.L., 2004, Eocene circulation of the Southern Ocean: Was Antarctica kept warm by
963 subtropical waters? *Paleoceanography*, v. 19, no. 4, p. n/a-n/a, doi: 10.1029/2004PA001014.

964 Huck, C.E., van de Flierdt, T., Bohaty, S.M., and Hammond, S.J., 2017, Antarctic climate, Southern
965 Ocean circulation patterns, and deep water formation during the Eocene: *Paleoceanography*, v.
966 32, no. 7, p. 674–691, doi: 10.1002/2017PA003135.

967 Hurley, S.J., Elling, F.J., Könneke, M., Buchwald, C., Wanke, S.D., Santoro, A.E., Lipp, J.S.,
968 Hinrichs, K.-U., and Pearson, A., 2016, Influence of ammonia oxidation rate on thaumarchaeal
969 lipid composition and the TEX86 temperature proxy: *Proceedings of the National Academy of
970 Sciences*, v. 113, no. 28, p. 7762–7767, doi: 10.1073/pnas.1518534113.

971 Hurley, S.J., Lipp, J.S., Close, H.G., Hinrichs, K.U., and Pearson, A., 2018, Distribution and export of
972 isoprenoid tetraether lipids in suspended particulate matter from the water column of the Western
973 Atlantic Ocean: *Organic Geochemistry*, v. 116, p. 90–102, doi:
974 10.1016/j.orggeochem.2017.11.010.

975 Hurdeman, E.P., Frieling, J., Reichgelt, T., Bijl, P.K., Bohaty, S.M., Holdgate, G.R., Gallagher, S.J.,
976 Peterse, F., Greenwood, D.R., and Pross, J., 2021, Rapid expansion of meso-megathermal rain
977 forests into the southern high latitudes at the onset of the Paleocene-Eocene Thermal Maximum:

978 Geology, doi: 10.1130/G47343.1.

979 Inglis, G.N., Farnsworth, A., Collinson, M.E., Carmichael, M.J., Naafs, B.D.A., Lunt, D.J., Valdes,
980 P.J., Pancost, R.D., Matthew, J., Lunt, D.J., Valdes, P.J., Pancost, D., and Unit, O.G., 2019,
981 Terrestrial environmental change across the onset of the PETM and the associated impact on
982 biomarker proxies : a cautionary tale: *Global and Planetary Change*, v. 181, no. July, p. 102991,
983 doi: 10.1016/j.gloplacha.2019.102991.

984 Inglis, G.N., Farnsworth, A., Lunt, D.J., Foster, G.L., Hollis, C.J., Pagani, M., Jardine, P.E., Pearson,
985 P.N., Markwick, P.J., Galsworthy, A.M.J., Raynham, L., Taylor, K.W.R., and Pancost, R.D.,
986 2015, Descent towards the Icehouse: Eocene sea surface cooling inferred from GDGT
987 distributions: *Paleoceanography*, v. 30, no. 7, p. 1000–1020, doi: 10.1002/2014PA002723.

988 John, C.M., Banerjee, N.R., Longstaffe, F.J., Sica, C., Law, K.R., and Zachos, J.C., 2012, Clay
989 assemblage and oxygen isotopic constraints on the weathering response to the Paleocene-Eocene
990 thermal maximum, East Coast of North America: *Geology*, v. 40, no. 7, p. 591–594, doi:
991 10.1130/G32785.1.

992 De Jonge, C., Hopmans, E.C., Zell, C.I., Kim, J.-H., Schouten, S., and Sinninghe Damsté, J.S., 2014,
993 Occurrence and abundance of 6-methyl branched glycerol dialkyl glycerol tetraethers in soils:
994 Implications for palaeoclimate reconstruction: *Geochimica et Cosmochimica Acta*, v. 141, p. 97–
995 112, doi: 10.1016/j.gca.2014.06.013.

996 Judd, E.J., Bhattacharya, T., and Ivany, L.C., 2020, A Dynamical Framework for Interpreting Ancient
997 Sea Surface Temperatures: *Geophysical Research Letters*, v. 47, no. 15, doi:
998 10.1029/2020GL089044.

999 Kim, J.H., van der Meer, J., Schouten, S., Helmke, P., Willmott, V., Sangiorgi, F., Koç, N., Hopmans,
1000 E.C., and Damsté, J.S.S., 2010, New indices and calibrations derived from the distribution of
1001 crenarchaeal isoprenoid tetraether lipids: Implications for past sea surface temperature
1002 reconstructions: *Geochimica et Cosmochimica Acta*, v. 74, no. 16, p. 4639–4654, doi:
1003 10.1016/j.gca.2010.05.027.

1004 Kim, J.H., Schouten, S., Rodrigo-Gámiz, M., Rampen, S., Marino, G., Hugué, C., Helmke, P., Buscail,
1005 R., Hopmans, E.C., Pross, J., Sangiorgi, F., Middelburg, J.B.M., and Sinninghe Damsté, J.S.,
1006 2015, Influence of deep-water derived isoprenoid tetraether lipids on the TEX86H
1007 paleothermometer in the Mediterranean Sea: *Geochimica et Cosmochimica Acta*, v. 150, p. 125–
1008 141, doi: 10.1016/j.gca.2014.11.017.

1009 Kirkels, F.M.S.A., Usman, M.O., and Peterse, F., 2022, Distinct sources of bacterial branched GMGTs
1010 in the Godavari River basin (India) and Bay of Bengal sediments: *Organic Geochemistry*, v. 167,
1011 no. February, p. 104405, doi: 10.1016/j.orggeochem.2022.104405.

1012 De La Torre, J.R., Walker, C.B., Ingalls, A.E., Könneke, M., and Stahl, D.A., 2008, Cultivation of a
1013 thermophilic ammonia oxidizing archaeon synthesizing crenarchaeol: *Environmental*
1014 *Microbiology*, v. 10, no. 3, p. 810–818, doi: 10.1111/j.1462-2920.2007.01506.x.

1015 Lagabriele, Y., Goddérès, Y., Donnadiou, Y., Malavieille, J., and Suarez, M., 2009, The tectonic
1016 history of Drake Passage and its possible impacts on global climate: *Earth and Planetary Science*
1017 *Letters*, v. 279, no. 3–4, p. 197–211, doi: 10.1016/j.epsl.2008.12.037.

1018 van de Lagemaat, S.H.A., Swart, M.L.A., Vaes, B., Kosters, M.E., Boschman, L.M., Burton-Johnson,
1019 A., Bijl, P.K., Spakman, W., and van Hinsbergen, D.J.J., 2021, Subduction initiation in the Scotia
1020 Sea region and opening of the Drake Passage: When and why? *Earth-Science Reviews*, p.
1021 103551, doi: 10.1016/j.earscirev.2021.103551.

1022 Lauretano, V., Littler, K., Polling, M., Zachos, J.C., and Lourens, L.J., 2015, Frequency, magnitude
1023 and character of hyperthermal events at the onset of the Early Eocene Climatic Optimum:
1024 *Climate of the Past*, v. 11, no. 10, p. 1313–1324, doi: 10.5194/cp-11-1313-2015.

1025 Liu, X.L., Summons, R.E., and Hinrichs, K.U., 2012, Extending the known range of glycerol ether
1026 lipids in the environment: Structural assignments based on tandem mass spectral fragmentation
1027 patterns: *Rapid Communications in Mass Spectrometry*, v. 26, no. 19, p. 2295–2302, doi:
1028 10.1002/rcm.6355.

1029 Lunt, D.J., Bragg, F., Chan, W.-L., Hutchinson, D.K., Ladant, J.-B., Morozova, P., Niezgodzki, I.,
1030 Steinig, S., Zhang, Z., Zhu, J., Abe-Ouchi, A., Anagnostou, E., de Boer, A.M., Coxall, H.K., et
1031 al., 2021, DeepMIP: model intercomparison of early Eocene climatic optimum (EECO) large-
1032 scale climate features and comparison with proxy data: *Climate of the Past*, v. 17, no. 1, p. 203–
1033 227, doi: 10.5194/cp-17-203-2021.

1034 Lunt, D.J., Farnsworth, A., Loptson, C., L Foster, G., Markwick, P., O'Brien, C.L., Pancost, R.D.,
1035 Robinson, S.A., and Wrobel, N., 2016, Palaeogeographic controls on climate and proxy
1036 interpretation: *Climate of the Past*, v. 12, no. 5, p. 1181–1198, doi: 10.5194/cp-12-1181-2016.

1037 Lunt, D.J., Huber, M., Anagnostou, E., Baatsen, M.L.J., Caballero, R., DeConto, R., Dijkstra, H.A.,

1038 Donnadieu, Y., Evans, D., Feng, R., Foster, G.L., Gasson, E., von der Heydt, A.S., Hollis, C.J., et
1039 al., 2017, The DeepMIP contribution to PMIP4: experimental design for model simulations of
1040 the EECO, PETM, and pre-PETM (version 1.0): *Geoscientific Model Development*, v. 10, no. 2,
1041 p. 889–901, doi: 10.5194/gmd-10-889-2017.

1042 McNerney, F.A., and Wing, S.L., 2011, The Paleocene-Eocene thermal maximum: a perturbation of
1043 carbon cycle, climate, and biosphere with implications for the future: *Annual Review of Earth
1044 and Planetary Sciences*, v. 39, no. 1, p. 489–516, doi: 10.1146/annurev-earth-040610-133431.

1045 Morii, H., Eguchi, T., Nishihara, M., Kakinuma, K., König, H., and Koga, Y., 1998, A novel ether core
1046 lipid with H-shaped C80-isoprenoid hydrocarbon chain from the hyperthermophilic methanogen
1047 *Methanothermus fervidus*: *Biochimica et Biophysica Acta - Lipids and Lipid Metabolism*, v.
1048 1390, no. 3, p. 339–345, doi: 10.1016/S0005-2760(97)00183-5.

1049 Müller, R.D., Zahirovic, S., Williams, S.E., Cannon, J., Seton, M., Bower, D.J., Tetley, M.G., Heine,
1050 C., Le Breton, E., Liu, S., Russell, S.H.J., Yang, T., Leonard, J., and Gurnis, M., 2019, A Global
1051 Plate Model Including Lithospheric Deformation Along Major Rifts and Orogens Since the
1052 Triassic: *Tectonics*, v. 38, no. 6, p. 1884–1907, doi: 10.1029/2018TC005462.

1053 Naafs, B.D.A., Inglis, G.N., Zheng, Y., Amesbury, M.J., Biester, H., Bindler, R., Blewett, J., Burrows,
1054 M.A., del Castillo Torres, D., Chambers, F.M., Cohen, A.D., Evershed, R.P., Feakins, S.J.,
1055 Gallego-Sala, A., et al., 2017, Introducing global peat-specific temperature and pH calibrations
1056 based on brGDGT bacterial lipids: *Geochimica et Cosmochimica Acta*, v. 208, no. June 2016, p.
1057 285–301, doi: 10.1016/j.gca.2017.01.038.

1058 Naafs, B.D.A., McCormick, D., Inglis, G.N., and Pancost, R.D., 2018a, Archaeal and bacterial H-
1059 GDGTs are abundant in peat and their relative abundance is positively correlated with
1060 temperature: *Geochimica et Cosmochimica Acta*, v. 227, p. 156–170, doi:
1061 10.1016/j.gca.2018.02.025.

1062 Naafs, B.D.A., Rohrsen, M., Inglis, G.N., Lääteenoja, O., Feakins, S.J., Collinson, M.E., Kennedy,
1063 E.M., Singh, P.K., Singh, M.P., Lunt, D.J., and Pancost, R.D., 2018b, High temperatures in the
1064 terrestrial mid-latitudes during the early Palaeogene: *Nature Geoscience*, v. 11, no. 10, p. 766–
1065 771, doi: 10.1038/s41561-018-0199-0.

1066 Nootboom, P.D., Baatsen, M., Bijl, P.K., Michael, A., Sebille, E. Van, Sluijs, A., and Dijkstra, H.A.,
1067 2021, Strongly eddying ocean simulations required to resolve Eocene model-data mismatch: , p.
1068 1–23, doi: 10.1002/essoar.10508749.1.

1069 Nootboom, P.D., Delandmeter, P., van Sebille, E., Bijl, P.K., Dijkstra, H.A., and von der Heydt, A.S.,
1070 2020, Resolution dependency of sinking Lagrangian particles in ocean general circulation
1071 models: *PLoS ONE*, v. 15, no. 9 September, p. 1–16, doi: 10.1371/journal.pone.0238650.

1072 O'Brien, C.L., Robinson, S.A., Pancost, R.D., Sinninghe Damsté, J.S., Schouten, S., Lunt, D.J.,
1073 Alsenz, H., Bornemann, A., Bottini, C., Brassell, S.C., Farnsworth, A., Forster, A., Huber, B.T.,
1074 Inglis, G.N., et al., 2017, Cretaceous sea-surface temperature evolution: Constraints from TEX
1075 86 and planktonic foraminiferal oxygen isotopes: *Earth-Science Reviews*, v. 172, no. March
1076 2016, p. 224–247, doi: 10.1016/j.earscirev.2017.07.012.

1077 Pak, D.K., and Miller, K.G., 1992, Paleocene to Eocene benthic foraminiferal isotopes and
1078 assemblages: implications for deepwater circulation: *Paleoceanography*, v. 7, no. 4, p. 405–422.

1079 Pancost, R.D., Taylor, K.W.R., Inglis, G.N., Kennedy, E.M., Handley, L., Hollis, C.J., Crouch, E.M.,
1080 Pross, J., Huber, M., Schouten, S., Pearson, P.N., Morgans, H.E.G., and Raine, J.I., 2013, Early
1081 Paleogene evolution of terrestrial climate in the SW Pacific, Southern New Zealand:
1082 *Geochemistry, Geophysics, Geosystems*, v. 14, no. 12, p. 5413–5429, doi:
1083 10.1002/2013GC004935.

1084 Pitcher, A., Villanueva, L., Hopmans, E.C., Schouten, S., Reichart, G.J., and Sinninghe Damsté, J.S.,
1085 2011, Niche segregation of ammonia-oxidizing archaea and anammox bacteria in the Arabian
1086 Sea oxygen minimum zone: *ISME Journal*, v. 5, no. 12, p. 1896–1904, doi:
1087 10.1038/ismej.2011.60.

1088 Prebble, J.G., Crouch, E.M., Carter, L., Cortese, G., Bostock, H., and Neil, H., 2013, An expanded
1089 modern dinoflagellate cyst dataset for the Southwest Pacific and Southern Hemisphere with
1090 environmental associations: *Marine Micropaleontology*, v. 101, p. 33–48, doi:
1091 10.1016/j.marmicro.2013.04.004.

1092 Pross, J., Contreras, L., Bijl, P.K., Greenwood, D.R., Bohaty, S.M., Schouten, S., Bendle, J.A.P., Röhl,
1093 U., Tauxe, L., Raine, J.I., Huck, C.E., Van De Flierdt, T., Jamieson, S.S.R., Stickley, C.E., et al.,
1094 2012, Persistent near-tropical warmth on the Antarctic continent during the early Eocene epoch:
1095 *Nature*, v. 487, no. 7409, p. 73–77, doi: 10.1038/nature11300.

1096 Reichgelt, T., Greenwood, D.R., Steinig, S., Conran, J.G., Hutchinson, D.K., Lunt, D.J., Scriven, L.J.,
1097 and Zhu, J., 2022, Plant Proxy Evidence for High Rainfall and Productivity in the Eocene of

1098 Australia:

1099 Reichgelt, T., West, C.K., and Greenwood, D.R., 2018, The relation between global palm distribution
1100 and climate: *Scientific Reports*, v. 8, no. 1, p. 4721, doi: 10.1038/s41598-018-23147-2.

1101 Sauermilch, I., Whittaker, J.M., Bijl, P.K., Totterdell, J.M., and Jokat, W., 2019, Tectonic,
1102 Oceanographic, and Climatic Controls on the Cretaceous-Cenozoic Sedimentary Record of the
1103 Australian-Antarctic Basin: *Journal of Geophysical Research: Solid Earth*, v. 124, no. 8, p. 7699–
1104 7724, doi: 10.1029/2018JB016683.

1105 Sauermilch, I., Whittaker, J.M., Klocker, A., Munday, D.R., Hochmuth, K., Bijl, P.K., and LaCasce,
1106 J.H., 2021, Gateway-driven weakening of ocean gyres leads to Southern Ocean cooling: *Nature*
1107 *Communications*, v. 12, no. 1, p. 1–8, doi: 10.1038/s41467-021-26658-1.

1108 Schneider-Mor, A., and Bowen, G.J., 2013, Coupled and decoupled responses of continental and
1109 marine organic-sedimentary systems through the Paleocene-Eocene thermal maximum, New
1110 Jersey margin, USA: *Paleoceanography*, v. 28, no. 1, p. 105–115, doi: 10.1002/palo.20016.

1111 Schouten, S., Baas, M., Hopmans, E.C., Reysenbach, A.L., and Damsté, J.S.S., 2008, Tetraether
1112 membrane lipids of *Candidatus "Aciduliprofundum boonei"*, a cultivated obligate
1113 thermoacidophilic euryarchaeote from deep-sea hydrothermal vents: *Extremophiles*, v. 12, no. 1,
1114 p. 119–124, doi: 10.1007/s00792-007-0111-0.

1115 Schouten, S., Hopmans, E.C., Schefuß, E., and Sinninghe Damsté, J.S., 2002, Distributional variations
1116 in marine crenarchaeotal membrane lipids: a new tool for reconstructing ancient sea water
1117 temperatures? *Earth and Planetary Science Letters*, v. 204, no. 1–2, p. 265–274, doi:
1118 10.1016/S0012-821X(02)00979-2.

1119 Schouten, S., Hopmans, E.C., and Sinninghe Damsté, J.S., 2013, The organic geochemistry of glycerol
1120 dialkyl glycerol tetraether lipids: A review: *Organic Geochemistry*, v. 54, no. 0, p. 19–61, doi:
1121 10.1016/j.orggeochem.2012.09.006.

1122 Secord, R., Gingerich, P.D., Lohmann, K.C., and MacLeod, K.G., 2010, Continental warming
1123 preceding the Palaeocene-Eocene thermal maximum: *Nature*, v. 467, no. 7318, p. 955–958, doi:
1124 10.1038/nature09441.

1125 Seton, M., Müller, R.D., Zahirovic, S., Gaina, C., Torsvik, T.H., Shephard, G., Talsma, A., Gurnis, M.,
1126 Turner, M., and Maus, S., 2012, Global continental and ocean basin reconstructions since
1127 200Ma: *Earth-Science Reviews*, v. 113, no. 3, p. 212–270.

1128 Sijp, W.P., England, M.H., and Huber, M., 2011, Effect of the deepening of the Tasman Gateway on
1129 the global ocean: *Paleoceanography*, v. 26, no. 4, p. 1–18, doi: 10.1029/2011PA002143.

1130 Sijp, W.P., von der Heydt, A.S., and Bijl, P.K., 2016, Model simulations of early westward flow across
1131 the Tasman Gateway during the early Eocene: *Climate of the Past*, v. 12, no. 4, p. 807–817, doi:
1132 10.5194/cp-12-807-2016.

1133 Sijp, W.P., von der Heydt, A.S., Dijkstra, H.A., Flögel, S., Douglas, P.M.J.J., and Bijl, P.K., 2014, The
1134 role of ocean gateways on cooling climate on long time scales: *Global and Planetary Change*, v.
1135 119, p. 1–22, doi: 10.1016/j.gloplacha.2014.04.004.

1136 Sinninghe Damsté, J.S., Irene C. Rijpstra, W., Hopmans, E.C., den Uijl, M.J., Weijers, J.W.H., and
1137 Schouten, S., 2018, The enigmatic structure of the crenarchaeol isomer: *Organic Geochemistry*,
1138 doi: 10.1016/j.orggeochem.2018.06.005.

1139 Sinninghe Damsté, J.S., Ossebaar, J., Schouten, S., and Verschuren, D., 2012, Distribution of tetraether
1140 lipids in the 25-ka sedimentary record of Lake Challa: Extracting reliable TEX 86 and
1141 MBT/CBT palaeotemperatures from an equatorial African lake: *Quaternary Science Reviews*, v.
1142 50, p. 43–54, doi: 10.1016/j.quascirev.2012.07.001.

1143 Sinninghe Damsté, J.S., Schouten, S., Hopmans, E.C., Van Duin, A.C.T., and Geenevasen, J.A.J.,
1144 2002, Crenarchaeol: The characteristic core glycerol dibiphytanyl glycerol tetraether membrane
1145 lipid of cosmopolitan pelagic crenarchaeota: *Journal of Lipid Research*, v. 43, no. 10, p. 1641–
1146 1651, doi: 10.1194/jlr.M200148-JLR200.

1147 Sluijs, A., Bijl, P.K., Schouten, S., Röhl, U., Reichert, G.-J., and Brinkhuis, H., 2011, Southern ocean
1148 warming, sea level and hydrological change during the Paleocene-Eocene thermal maximum:
1149 *Climate of the Past*, v. 7, no. 1, p. 47–61, doi: 10.5194/cp-7-47-2011.

1150 Sluijs, A., Brinkhuis, H., Schouten, S., Bohaty, S.M., John, C.M., Zachos, J.C., Reichert, G.-J.,
1151 Sinninghe Damsté, J.S., Crouch, E.M., and Dickens, G.R., 2007, Environmental precursors to
1152 rapid light carbon injection at the Palaeocene/Eocene boundary.: *Nature*, v. 450, no. 7173, p.
1153 1218–1221, doi: 10.1038/nature06400.

1154 Sluijs, A., Frieling, J., Inglis, G.N., Nierop, K.G.J., Peterse, F., Sangiorgi, F., and Schouten, S., 2020,
1155 Late Paleocene–early Eocene Arctic Ocean sea surface temperatures: reassessing biomarker
1156 paleothermometry at Lomonosov Ridge: *Climate of the Past*, v. 16, no. 6, p. 2381–2400, doi:
1157 10.5194/cp-16-2381-2020.

1158 Sutherland, R., Dickens, G.R., Blum, P., Agnini, C., Alegret, L., Asatryan, G., Bhattacharya, J.,
1159 Bordenave, A., Chang, L., Collot, J., Cramwinckel, M.J., Dallanave, E., Drake, M.K., Etienne,
1160 S.J.G., et al., 2019, Expedition 371 summary.

1161 Taylor, K.W.R., Huber, M., Hollis, C.J., Hernandez-Sanchez, M.T., and Pancost, R.D., 2013, Re-
1162 evaluating modern and Palaeogene GDGT distributions: Implications for SST reconstructions:
1163 Global and Planetary Change, v. 108, p. 158–174, doi: 10.1016/j.gloplacha.2013.06.011.

1164 Thomas, D.J., Zachos, J.C., Bralower, T.J., Thomas, E., and Bohaty, S.M., 2002, Warming the Fuel for
1165 the Fire : Evidence for the Thermal Dissociation of Methane Hydrate During the Paleocene-
1166 Eocene Thermal Maximum dissociation of methane hydrate during the Paleocene-Eocene:
1167 Geology, v. 30, no. 12, p. 1067–1070, doi: 10.1130/0091-
1168 7613(2002)030<1067:WTFFTF>2.0.CO;2.

1169 Tierney, J.E., and Tingley, M.P., 2015, A TEX86 surface sediment database and extended Bayesian
1170 calibration: Scientific Data, v. 2, p. 150029, doi: 10.1038/sdata.2015.29.

1171 Vahlenkamp, M., Niezgodzki, I., De Vleeschouwer, D., Lohmann, G., Bickert, T., and Pälike, H.,
1172 2018, Ocean and climate response to North Atlantic seaway changes at the onset of long-term
1173 Eocene cooling: Earth and Planetary Science Letters, v. 498, p. 185–195, doi:
1174 10.1016/j.epsl.2018.06.031.

1175 Weijers, J.W.H., Schouten, S., van den Donker, J.C., Hopmans, E.C., and Sinninghe Damsté, J.S.,
1176 2007, Environmental controls on bacterial tetraether membrane lipid distribution in soils:
1177 Geochimica et Cosmochimica Acta, v. 71, no. 3, p. 703–713, doi: 10.1016/j.gca.2006.10.003.

1178 Weijers, J.W.H., Schouten, S., Spaargaren, O.C., and Sinninghe Damsté, J.S., 2006, Occurrence and
1179 distribution of tetraether membrane lipids in soils: Implications for the use of the TEX86 proxy
1180 and the BIT index: Organic Geochemistry, v. 37, no. 12, p. 1680–1693, doi:
1181 10.1016/j.orggeochem.2006.07.018.

1182 Westerhold, T., Marwan, N., Drury, A.J., Liebrand, D., Agnini, C., Anagnostou, E., Barnet, J.S.K.,
1183 Bohaty, S.M., De Vleeschouwer, D., Florindo, F., Frederichs, T., Hodell, D.A., Holbourn, A.E.,
1184 Kroon, D., et al., 2020, An astronomically dated record of Earth’s climate and its predictability
1185 over the last 66 million years: Science, v. 369, no. 6509, p. 1383–1388, doi:
1186 10.1126/SCIENCE.ABA6853.

1187 Westerhold, T., Röhl, U., Donner, B., and Zachos, J.C., 2018, Global Extent of Early Eocene
1188 Hyperthermal Events: A New Pacific Benthic Foraminiferal Isotope Record From Shatsky Rise
1189 (ODP Site 1209): Paleoceanography and Paleoclimatology, v. 0, no. ja, p. 1–17, doi:
1190 10.1029/2017PA003306.

1191 Williams, G.L., Fensome, R.A., and MacRae, R.A., 2017, The Lentin and Williams index of fossil
1192 dinoflagellates 2017 edition.: American Association of Petroleum Geologists Contribution
1193 Series, v. 48.

1194 Williams, S.E., Whittaker, J.M., Halpin, J.A., and Müller, R.D., 2019, Australian-Antarctic breakup
1195 and seafloor spreading: Balancing geological and geophysical constraints: Earth-Science
1196 Reviews, v. 188, no. September 2018, p. 41–58, doi: 10.1016/j.earscirev.2018.10.011.

1197 Xie, S., Liu, X.-L., Schubotz, F., Wakeham, S.G., and Hinrichs, K.-U., 2014, Distribution of glycerol
1198 ether lipids in the oxygen minimum zone of the Eastern Tropical North Pacific Ocean: Organic
1199 Geochemistry, v. 71, p. 60–71, doi: 10.1016/j.orggeochem.2014.04.006.

1200 Zachos, J.C., Rohl, U., Schellenberg, S.A., Sluijs, A., Hodell, D.A., Kelly, D.C., Thomas, E., Nicolo,
1201 M.J., Raffi, I., Lourens, L.J., McCarren, H.K., and Kroon, D., 2005, Rapid Acidification of the
1202 Ocean During the Paleocene-Eocene Thermal Maximum: Science, v. 308, no. 5728, p. 1611–
1203 1615, doi: 10.1126/science.1109004.

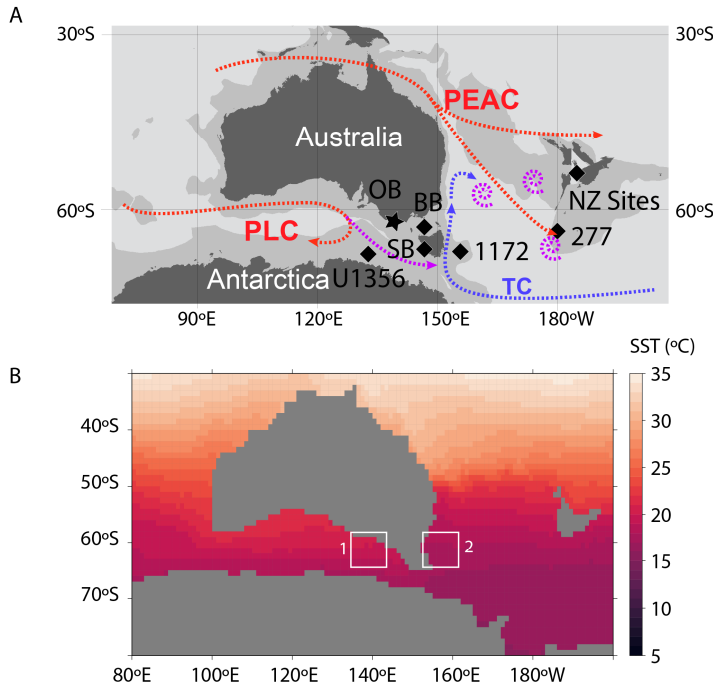
1204 Zhang, Y.G., Pagani, M., and Wang, Z., 2016, Ring Index: A new strategy to evaluate the integrity of
1205 TEX 86 paleothermometry: Paleoceanography, v. 31, no. 2, p. 220–232, doi:
1206 10.1002/2015PA002848.

1207 Zhang, Y.G., Zhang, C.L., Liu, X.L., Li, L., Hinrichs, K.U., and Noakes, J.E., 2011, Methane Index: A
1208 tetraether archaeal lipid biomarker indicator for detecting the instability of marine gas hydrates:
1209 Earth and Planetary Science Letters, v. 307, no. 3–4, p. 525–534, doi:
1210 10.1016/j.epsl.2011.05.031.

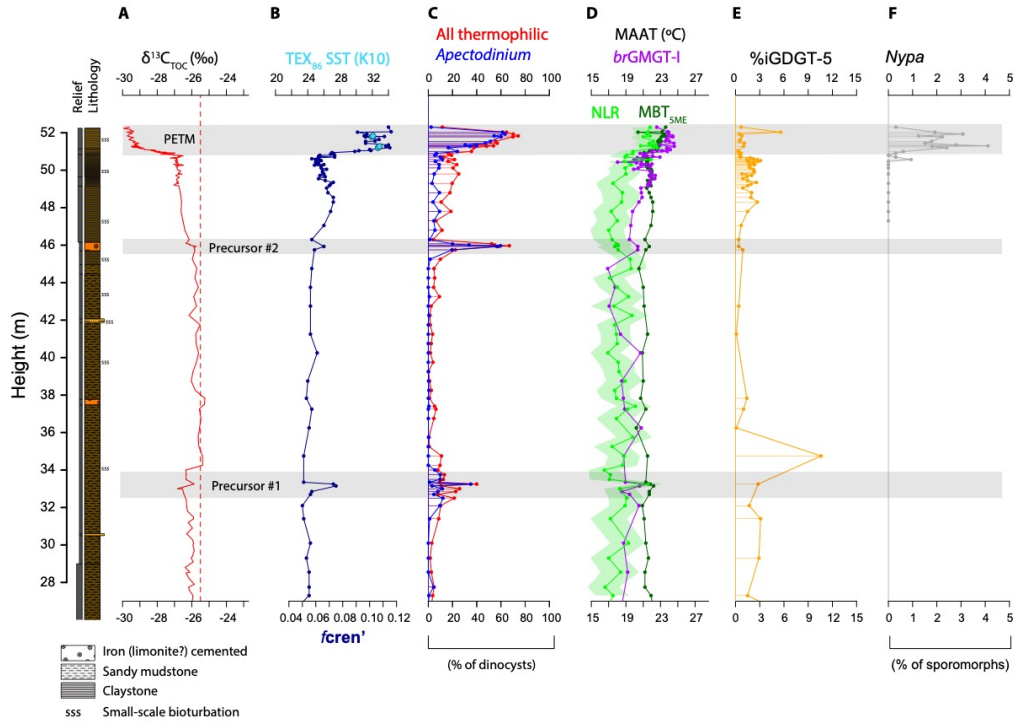
1211 Zhu, J., Poulsen, C.J., and Tierney, J.E., 2019, Simulation of Eocene extreme warmth and high climate
1212 sensitivity through cloud feedbacks: Science Advances, v. 5, no. 9, p. eaax1874, doi:
1213 10.1126/sciadv.aax1874.

1214 Zonneveld, K.A.F., Marret, F., Versteegh, G.J.M., Bogus, K., Bonnet, S., Bouimetarhan, I., Crouch, E.,
1215 de Vernal, A., Elshanawany, R., Edwards, L., Esper, O., Forke, S., Grøsfjeld, K., Henry, M., et
1216 al., 2013, Atlas of modern dinoflagellate cyst distribution based on 2405 data points: Review of
1217 Palaeobotany and Palynology, v. 191, p. 1–197, doi: 10.1016/j.revpalbo.2012.08.003.

1219 **Figures main text**
1220

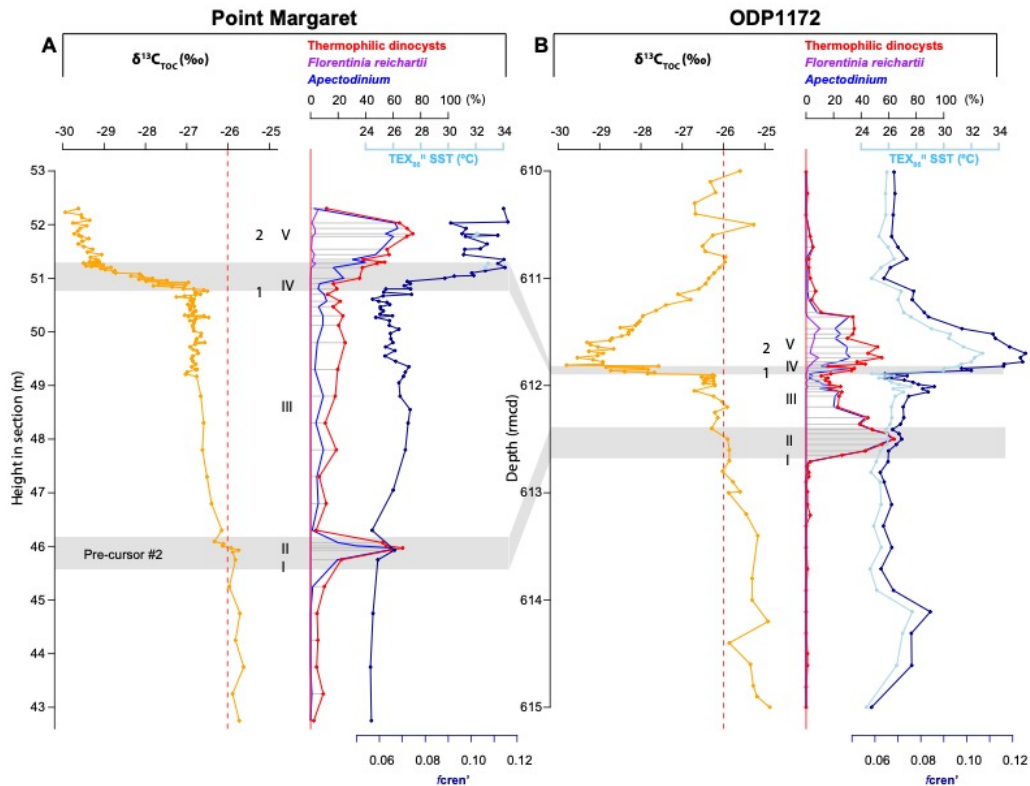


1221 **Figure 1. Paleogeographical reconstruction of the Tasman Gateway area around 56 Ma** (Müller et
1222 al., 2019). **A.** Location of Point Margaret and Latrobe-1 (star) and previously used sites (diamonds) for
1223 which data was generated and compiled, respectively. Abbreviations: OB = Otway Basin: Point
1224 Margaret and Latrobe-1. BB = Bass Basin (Konkon-1, Poonboon-1), SB=Sorrell Basin (Lowana
1225 Road), Tasmania, U1356 = IODP Site U1356, 1172 = ODP Site 1172, 277 = DSDP Site 277, NZ Sites
1226 = multiple sites in New Zealand (Mid-Waipara, Tora, Tawanui, Otaio River). For modern locations see
1227 Fig. S1. Other abbreviations: PLC = Proto-Leeuwin Current, TC = Tasman Current, PEAC = Proto
1228 East Australia Current. Biogeography and simplified model-based currents; red, purple and blue arrows
1229 indicate low-latitude, transitional and Antarctic-derived surface currents and eddies, respectively (Bijl
1230 et al., 2013a; Sauermilch et al., 2019; Nooteboom et al., 2021). **B.** Regional modeled sea surface
1231 temperature. Model run represents a high $p\text{CO}_2$ (6x pre-industrial $p\text{CO}_2$) of CESM1.2 (Zhu et al., 2019;
1232 Lunt et al., 2021). Note higher SST in the AAG (box 1) compared to the SW Pacific (box 2) at the
1233 same latitude.
1234
1235



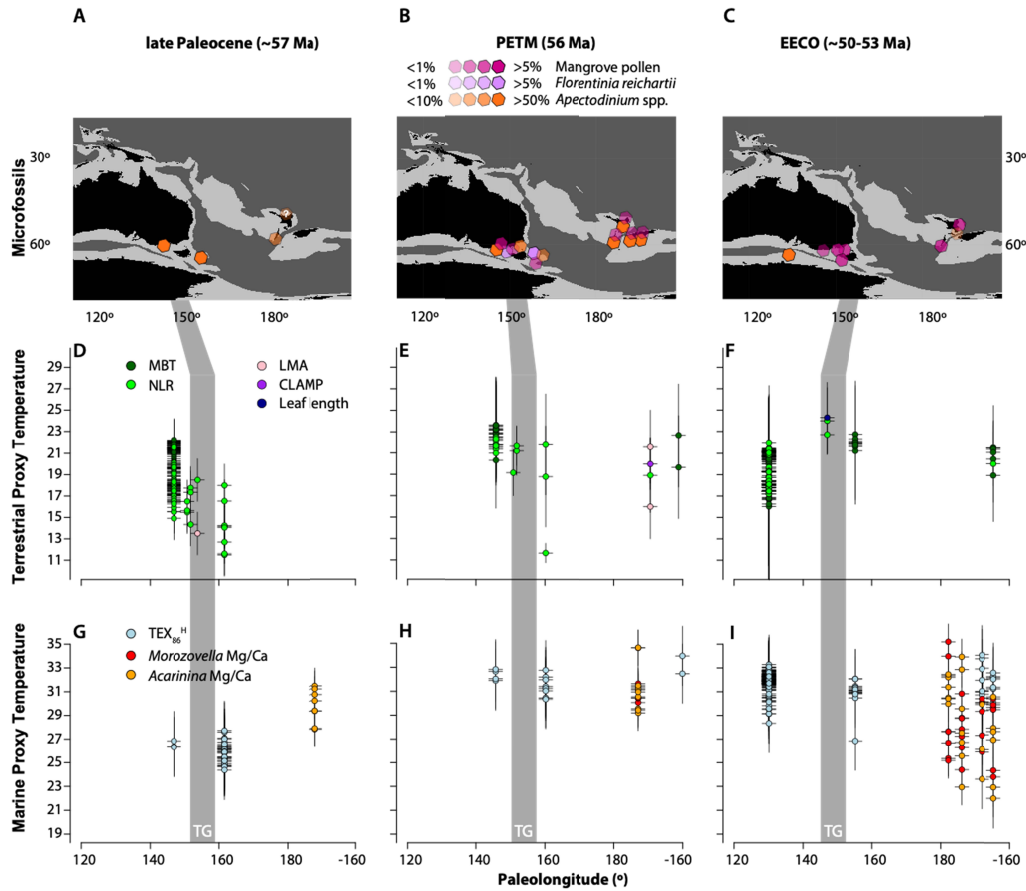
1237
 1238
 1239
 1240
 1241
 1242
 1243
 1244
 1245
 1246

Figure 2. Point Margaret late Paleocene and PETM proxy data. **A.** Biostratigraphy, bulk organic matter carbon isotope values ($\delta^{13}\text{C}_{\text{TOC}}$) and lithology from Frieling et al., (2018). **B.** SST trends from relative abundance of crenarchaeol stereoisomer to total crenarchaeol ($f(\text{cren}')^1$, this study) and TEX_{86} -based SST estimates. Note that the TEX_{86} dataset contains only 4 samples within the PETM CIE. **C.** %*Apectodinium* and %Thermophilic taxa of total dinocyst assemblage (this study). **D.** MAAT estimates based on MBT_{SME} , NLR (Hurdeman et al. 2021 & this study), and brGMGT-I (this study). **E.** %iGDGT-5 (this study). **F.** %*Nypa* of total pollen and spore assemblage (Hurdeman et al. 2021).



1247
 1248
 1249
 1250
 1251
 1252
 1253
 1254
 1255

Figure 3. Comparison of latest Paleocene - PETM temperature trends west and east of the Tasman Gateway A. Point Margaret. B. ODP Site 1172. Numbers and roman numerals next to isotope ($\delta^{13}C_{TOC}$) and dinocyst records refer to here correlated events: 1. Onset of the carbon isotope excursion. 2. Body of the carbon isotope excursion. I. Abundance of *Areoligera* complex. II. Abundance (acme) *Apectodinium*. III. Interval with common *Apectodinium*. IV. Abundance (acme) of *Apectodinium*. V. First consistent occurrence of *Florentinia reichartii*. Note that SST at Point Margaret is represented by only 4 TEX₈₆ estimates, and limited to the body of the CIE.



1257
1258
1264
1265
1266
1267
1268
1269

Figure 4: Proxy compilation across three time-slices; late Paleocene, PETM and EECO. A-C. Relative abundance of thermophilic microfossil taxa, mangrove pollen (*Nypa*) and dinocysts (*Apectodinium* and *Florentinia reichertii*), **D-F.** Terrestrial temperature reconstructions based on vegetation (dark green) and biomarkers (green). **G-I.** Sea surface temperature reconstructions using TEX_{86}^H (light blue), Mg/Ca of mixed-layer foraminifera *Acarinina* (orange) and *Morozovella* (red). Grey vertical band represents the Tasman Gateway (TG) area.

SST Proxy estimates			late Paleocene			PETM			EECO			Reference
Region	Site	Proxy	n=	mean	SE	n=	mean	SE	n=	mean	SE	Reference
SW Pacific	ODP1172	TEX86H	30	25.9	0.2	8	31.5	0.3	15	30.9	0.3	Bijl et al. 2009, 2013, 2021, Sluijs et al. 2011
		TEXLIN	30	27.2	0.2	8	35.1	0.6	15	34.2	0.5	
	Mid-Waipara	TEX86H				2	33.2	0.8	5	31.6	0.3	Pancost et al. 2013, Hollis et al. 2012
		TEXLIN							5	35.3	0.5	
	Hampden Beach	Mg/Ca Acarinina							4	26.3	1.3	Hollis et al. 2009, Hines et al. 2017, Inglis et al. 2015
			TEX86H							8	31.9	
		TEXLIN							8	35.9	0.8	
	DSDP277	Mg/Ca Morozovella							5	28.6	0.9	Hollis et al. 2015, Hines et al. 2017
		Mg/Ca Acarinina							3	26.6	1.8	
		Mg/Ca Morozovella				7	31.4	0.6	5	29.3	1.4	
Tora	Mg/Ca Acarinina		8	29.8	0.5	8	30.9	0.6	6	31.2	0.4	Hines et al. 2017
	Mg/Ca Morozovella							6	25.7	0.9		
Tawanui	Mg/Ca Morozovella							6	26.8	1.7	Hines et al. 2017	
		Mg/Ca Acarinina						1	27.2			
Australo-Antarctic Gulf	U1356A	TEX86H							131	31.9	0.1	Bijl et al. 2013
	TEXLIN							131	35.7	0.1		
Latrobe-1	TEX86H		2	27.3	0.2							This study
		TEXLIN	2	29	0.3							
	TEX86H	1	26.3		4	32.4	0.2				This study	
Point Margaret	TEXLIN				4	36.5	0.4					This study

MAAT Proxy estimates			late Paleocene			PETM			EECO			Reference	
Region	Site	Proxy	n=	mean	SE	n=	mean	SE	n=	mean	SE	Reference	
SW Pacific	ODP1172	MBT							9	21.9	0.1	Bijl et al. 2013, 2021	
		NLR	8	14.1	0.8	3	17.4	3.0					
	Mid-Waipara	MBT				2	21.2	1.5	6	20.8	0.4	Contreras et al. 2014	
		Coeistence							1	20.0			
	Konkon-1	NLR		3	16.5	1.1	2	21.4	0.2				Contreras et al. 2014
				3	15.9	0.3	1	19.2					
Poonboon-1	NLR		1	18.5								Contreras et al. 2014	
			1	13.5									
Cambalong creek	MA		1	13.5								Greenwood et al. 2003, Contreras et al. 2014	
Australo-Antarctic Gulf	Point Margaret	NLR	66	17.9	0.2	8	21.7	0.2				Huurdeeman et al. 2021 & this study	
		MBT	70	21.3	0.1	12	22.9	0.3					
	brGMGT-/		58	18.7	0.2	12	23.6	0.2				This study	
		NLR	6	19.7	0.1	1	22.3						
	Latrobe-1	NLR							62	20.1	0.2	Pross et al. 2012	
			MBT						81	18.4	0.1		
	U1356A	NLR							2	23.4	0.7	Carpenter et al. 2012	
									1	24.3			
	Lowana Road, Tasmania	Coeistence							1	20.0		Reichgelt et al. 2022	
			Podocarpus leaf length						1	22.6			
Deans Marsh	NLR							1	19.5		Reichgelt et al. 2022		
		CAMP						1	19.7				
Dinmore	NLR							1	19.7		Reichgelt et al. 2022		
		CAMP						1	18.9				

Semi-quantitative temperature estimates			late Paleocene			PETM			EECO			Reference
Region	Site	Proxy	minimum			minimum			minimum			Reference
SW Pacific	ODP1172	Dinocysts	20			25			25			Sluijs et al. 2011, Bijl et al. 2021
		Pollen				22						
	Mid-Waipara	Dinocysts				20						Contreras et al. 2014
		Dinocysts				20						
	Tawanui	Dinocysts				20						Crouch et al. 2014 & references therein
Kumara-2	Dinocysts				20						Crouch et al. 2014 & references therein	
Toi-Flat-1	Dinocysts				20						Crouch et al. 2014 & references therein	
Australo-Antarctic Gulf	Point Margaret	Dinocysts	20			25						This study
		Pollen				22						
	Latrobe-1	Dinocysts	20			25			20			Huurdeeman et al. (2021)
		Pollen				22			22			
Lowana Road, Tasmania	Pollen & Macrofossils							22			Carpenter et al. 2012	
								20				
U1356A	Dinocysts							20			Bijl et al. 2013	

1265
1272
1273
1274
1275
1276
1277
1278

Table 1. From top to bottom - SST, MAAT and semi-quantitative minimum temperature proxy estimates for the SW Pacific and AAG. Data sources: (Greenwood et al., 2003; Bijl et al., 2009; Hollis et al., 2009; Sluijs et al., 2011; Carpenter et al., 2012; Hollis et al., 2012; Pross et al., 2012; Bijl et al., 2013a; Pancost et al., 2013; Contreras et al., 2014; Crouch et al., 2014; Hollis et al., 2015; Inglis et al., 2015; Hines et al., 2017; Bijl et al., 2021; Huurdeman et al., 2021; Reichgelt et al., 2022)

Figure 1.

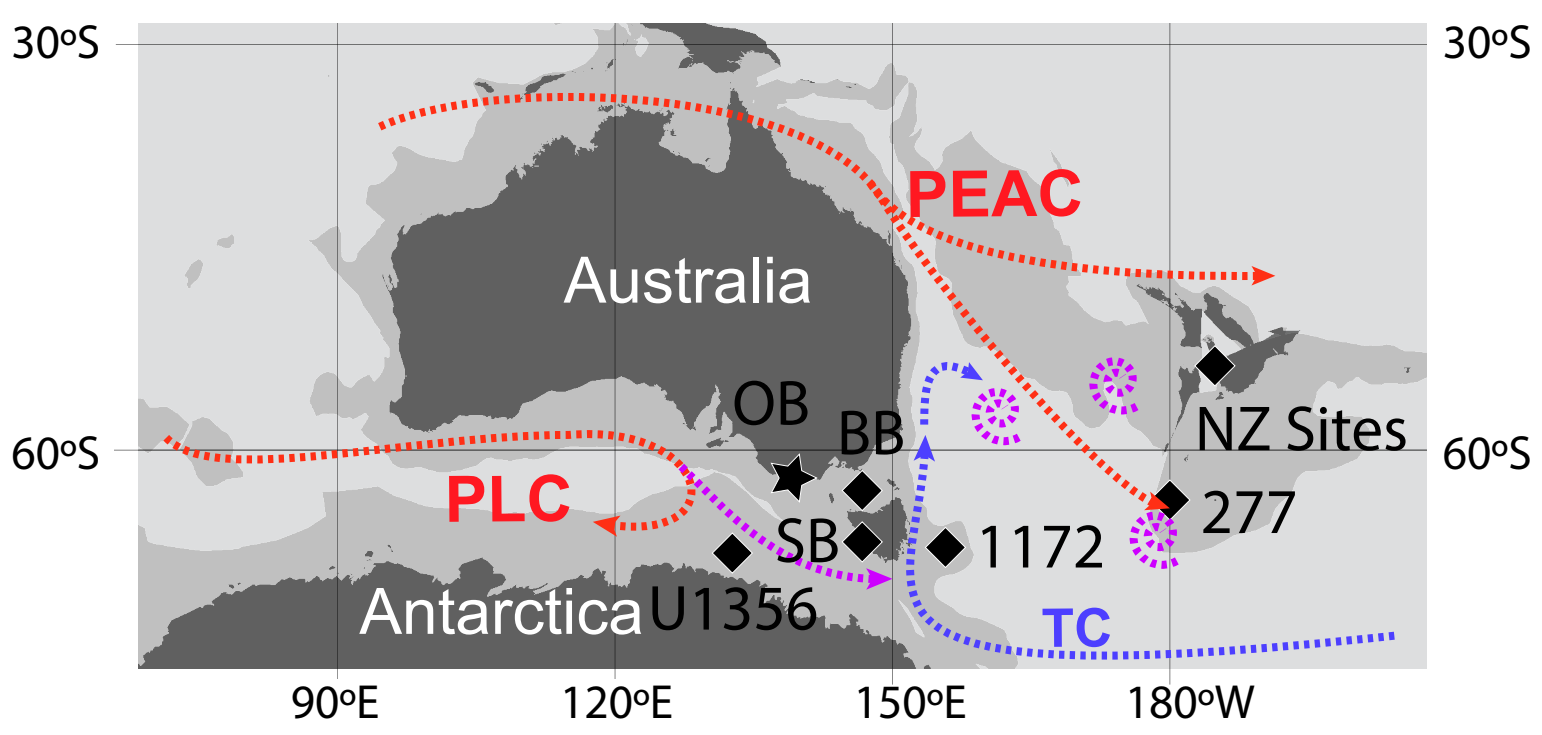


Figure 2.

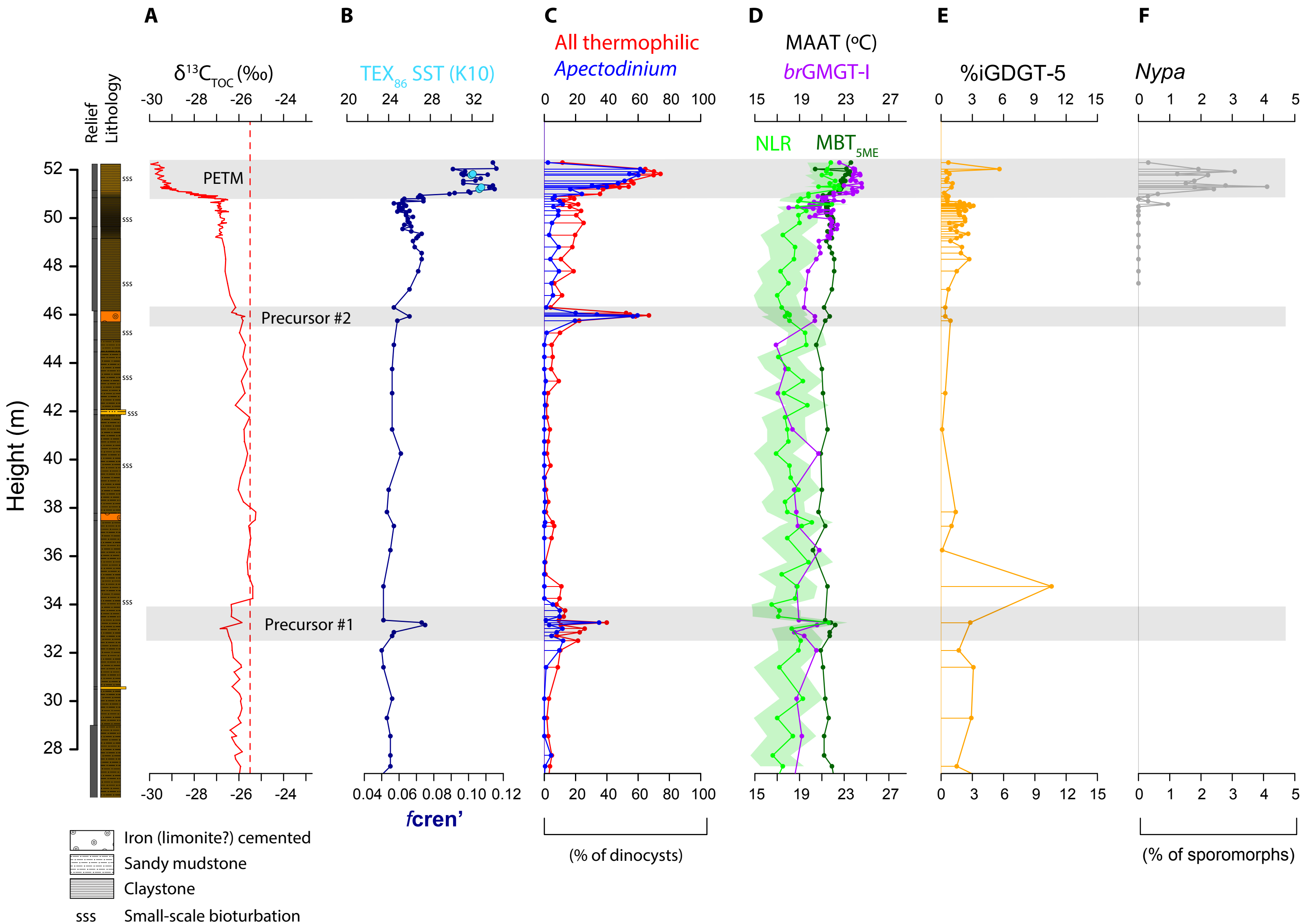
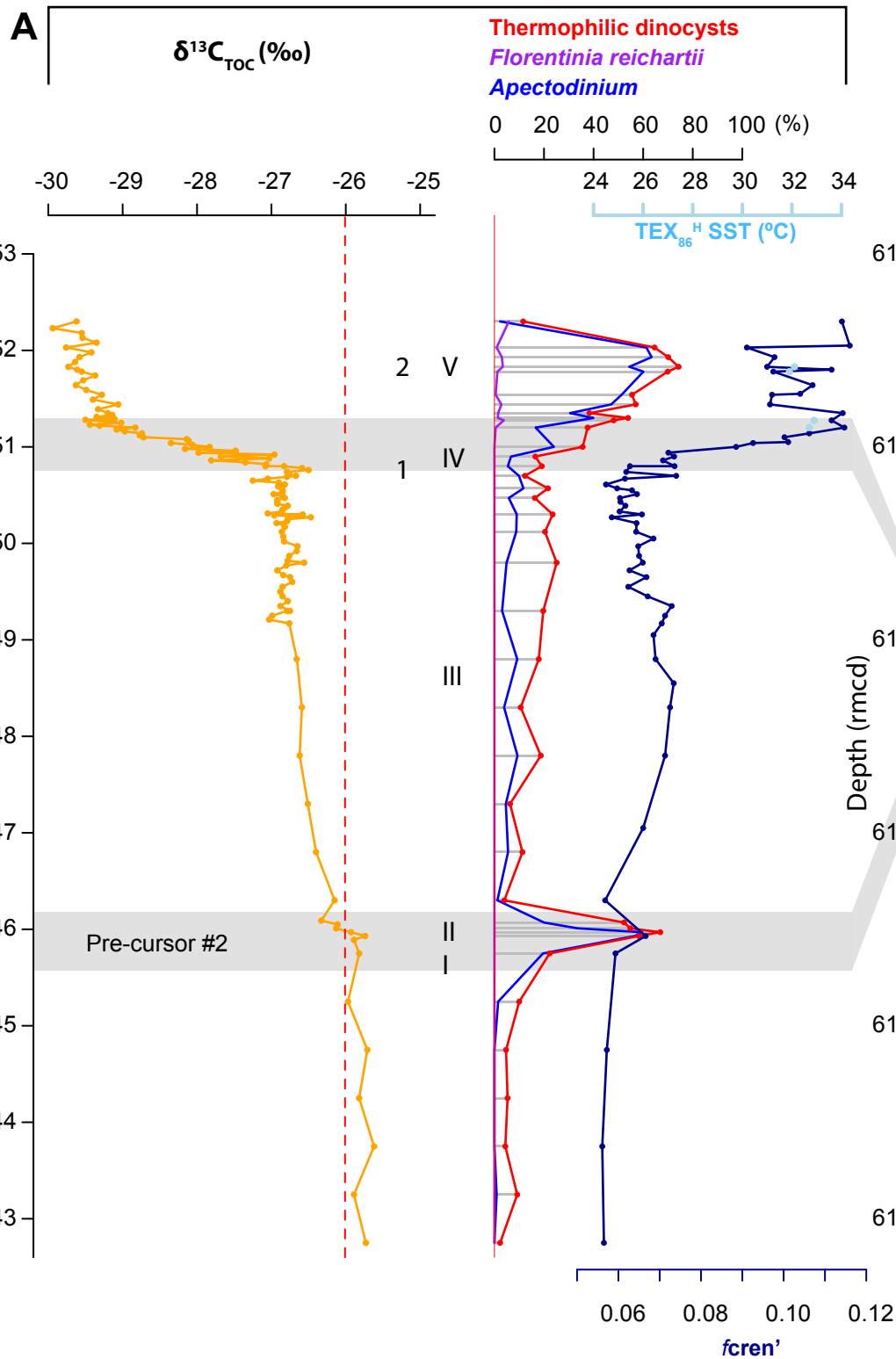


Figure 3.

Point Margaret



ODP1172

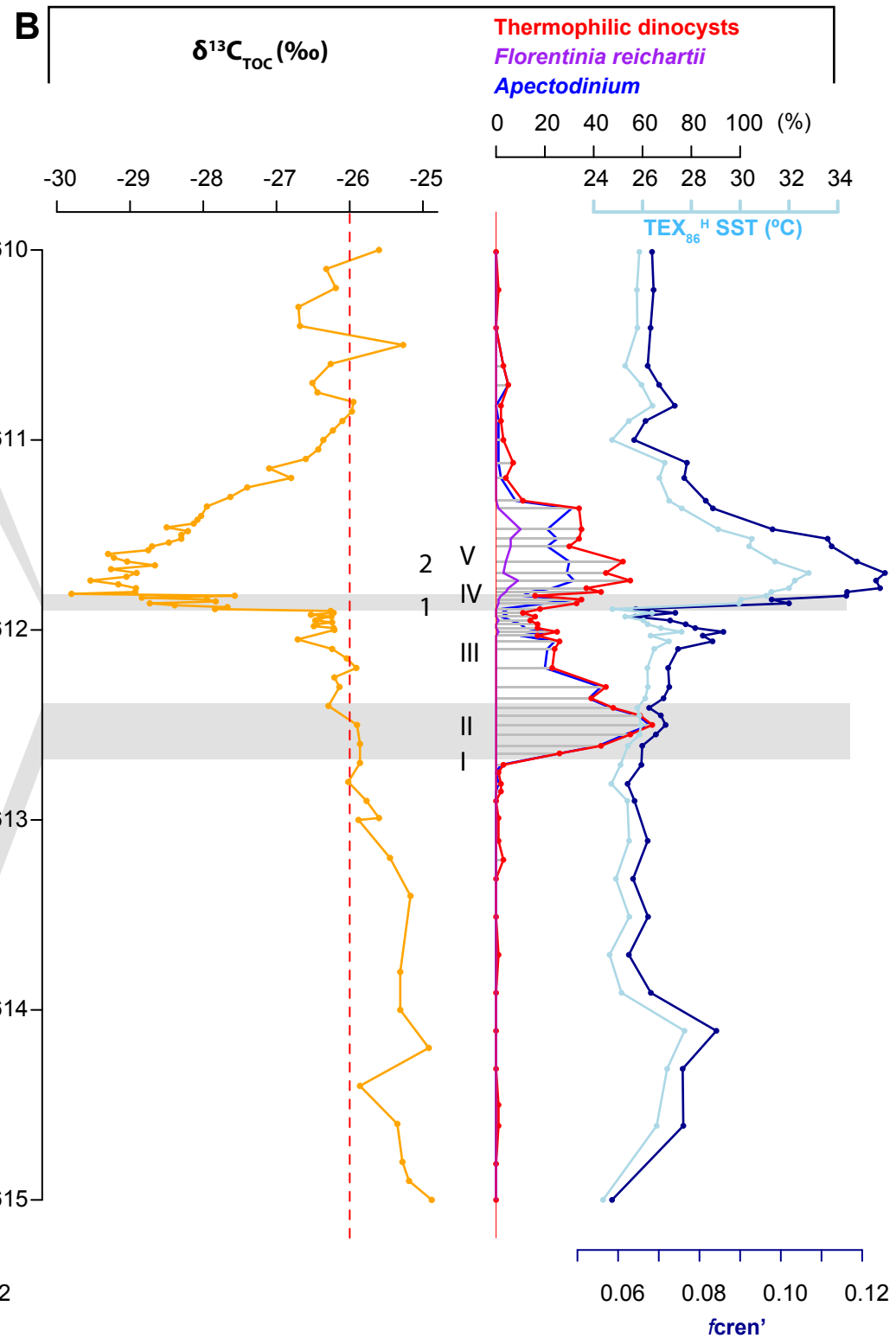
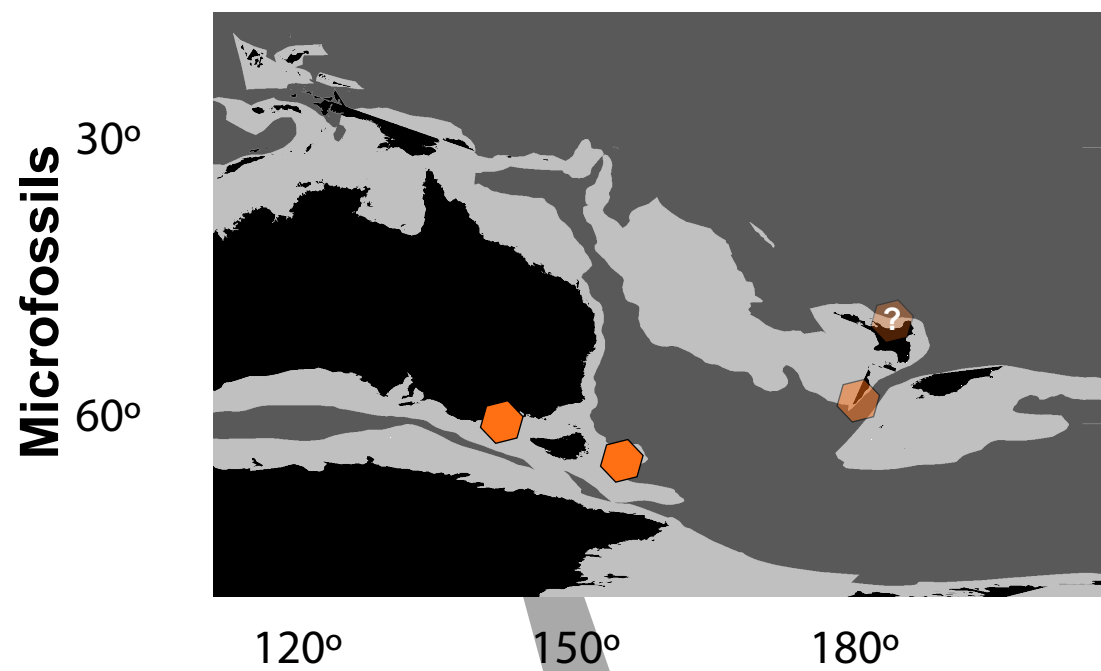
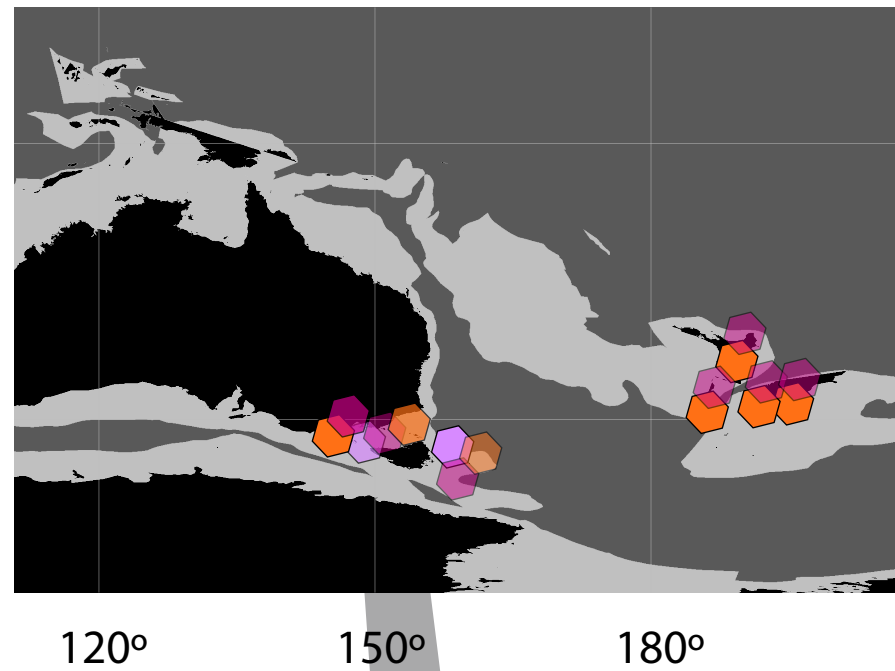
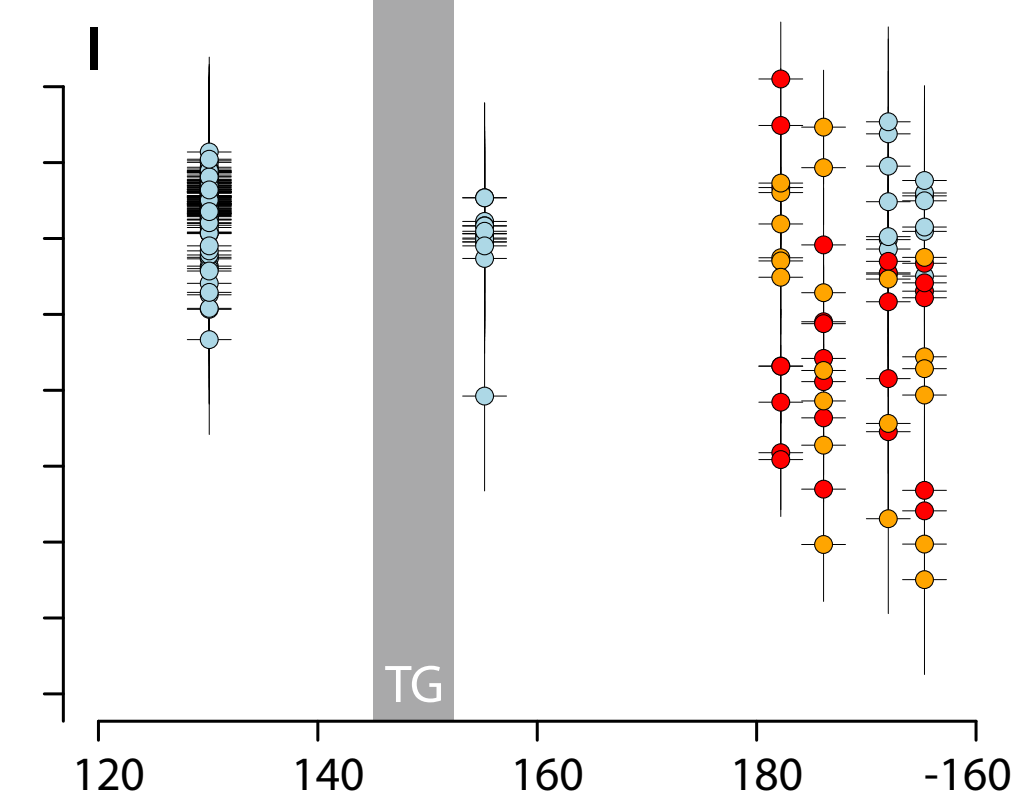
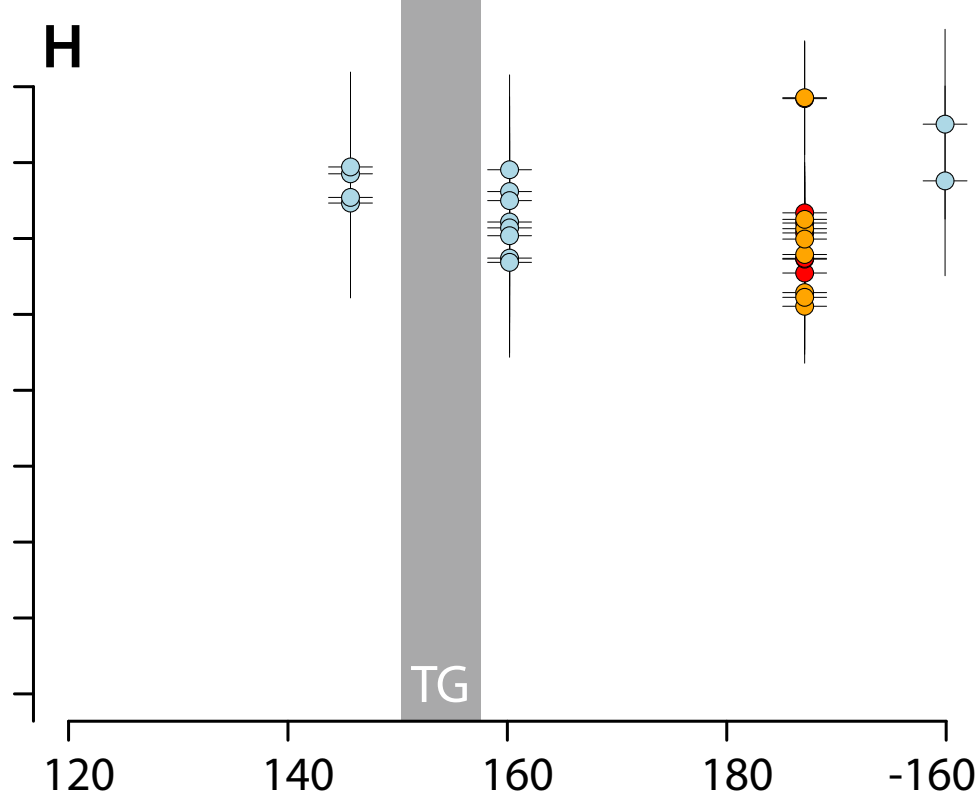
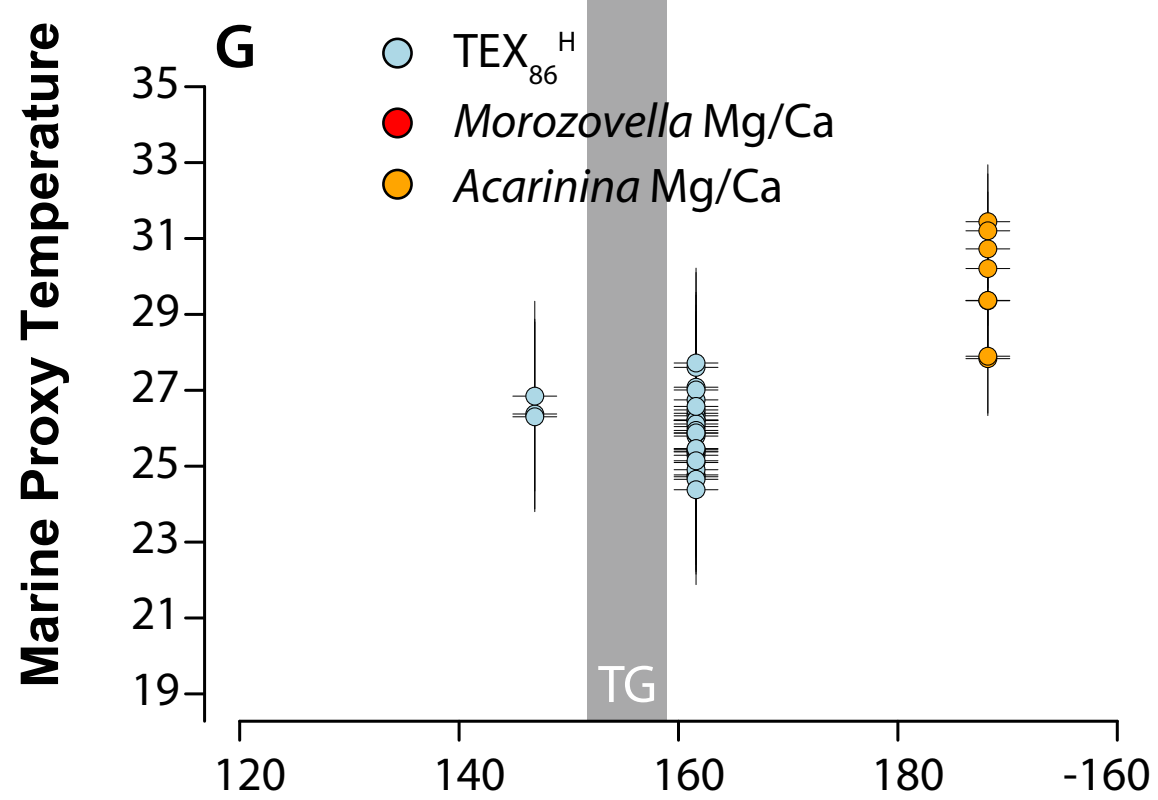
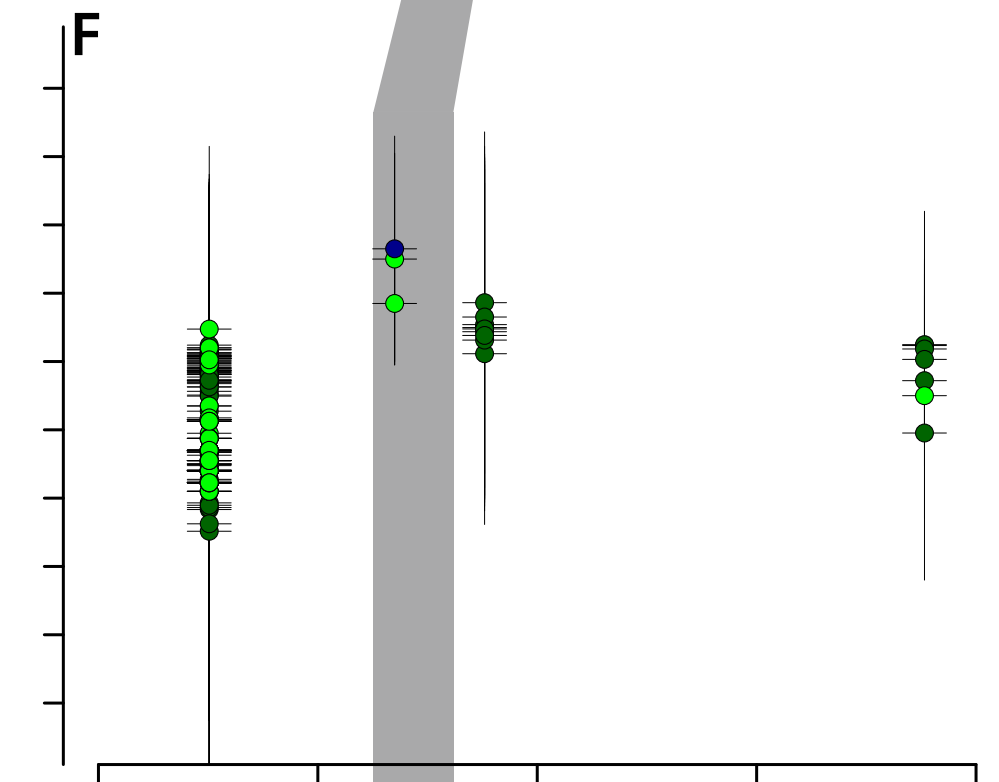
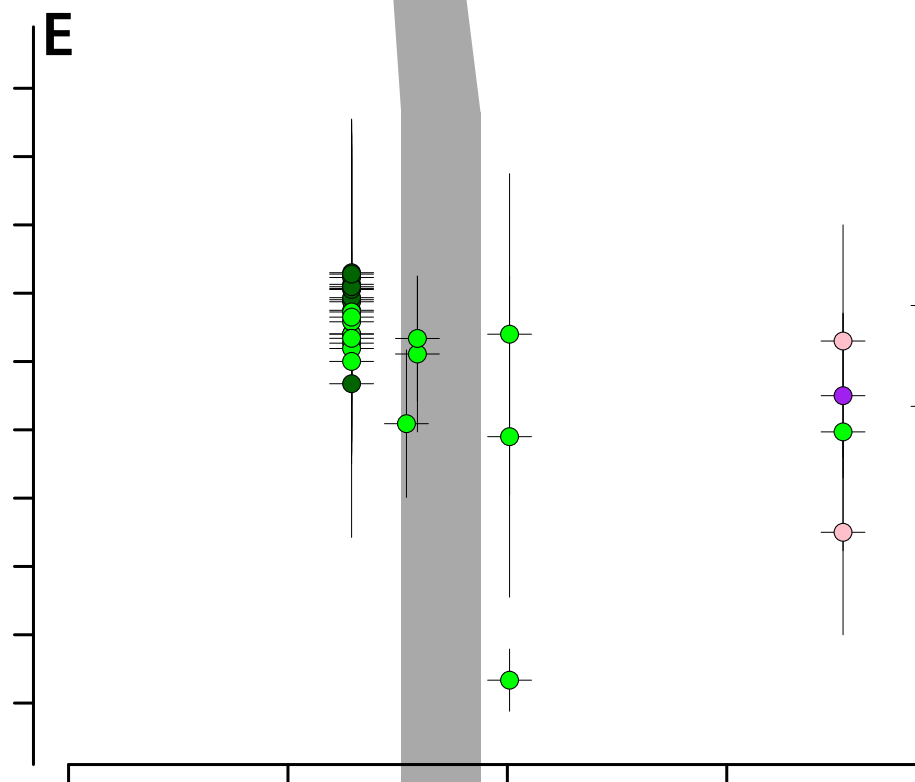
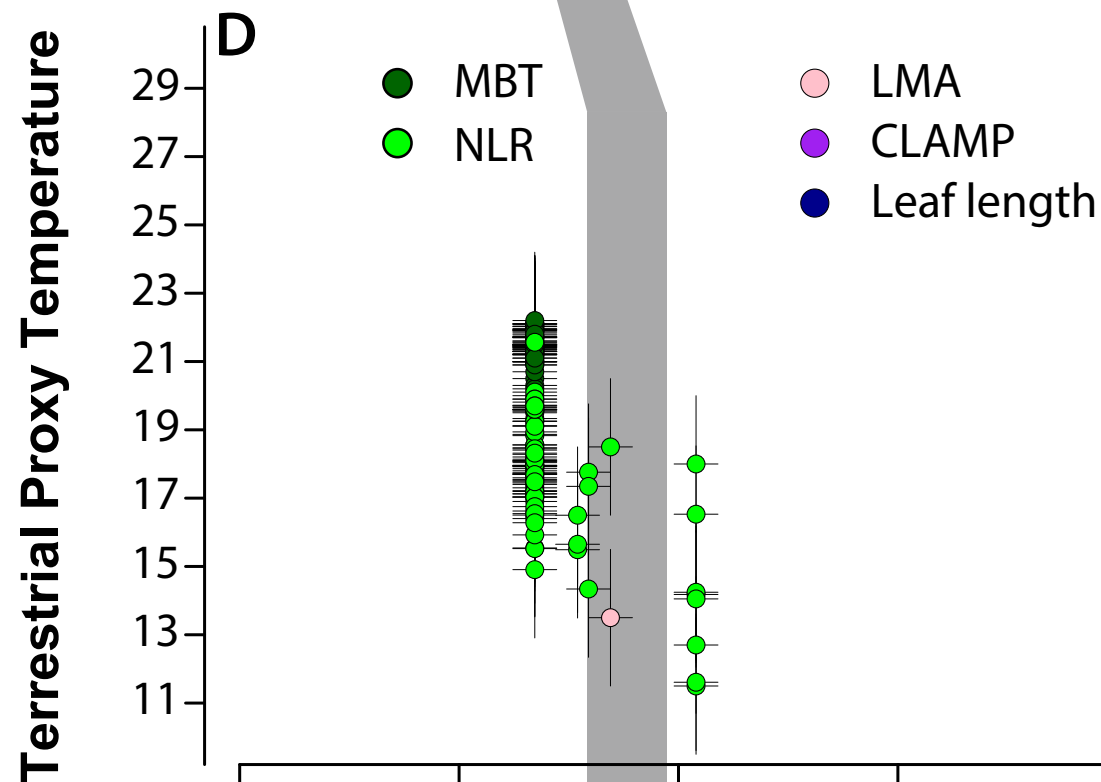
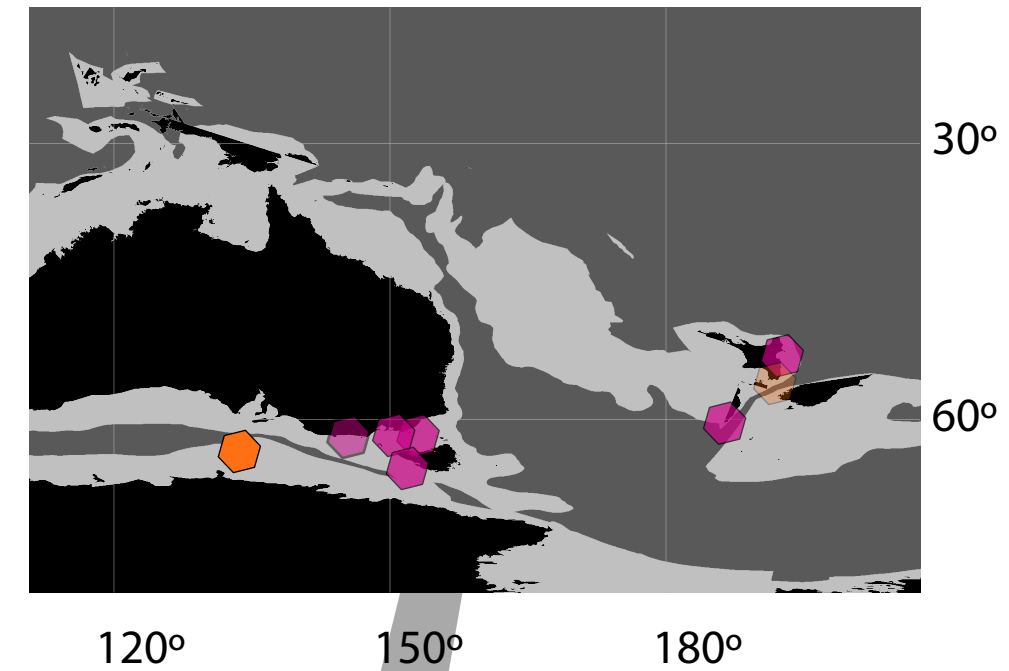


Figure 4.

A**late Paleocene (~57 Ma)****B****PETM (56 Ma)**

<1% >5% Mangrove pollen
 <1% >5% *Florentinia reichartii*
 <10% >50% *Apectodinium* spp.

**C****EECO (~50-53 Ma)****Paleolongitude (°)**